Thermal transitions, interfacial interactions, and molecular mobility in nanocomposites based on poly(l,d-lactic acid) and fumed silica nanoparticles

Panagiotis A. Klonos[1,2] · Evi Christodoulou[1] · Theodora C. Katsika[2] · Chrysanthi Papoulia[3] ·
Konstantinos Chrissafis[3] · Apostolos Kyritsis[2] · Dimitrios N. Bikiaris[1]

Abstract

We investigate the direct and indirect effects of silica nanoparticles, NP, on the molecular mobility and crystallization of a series of polymer nanocomposites, PNCs, based on polylactide, PLA. To that aim, a sum of complementary techniques was employed, namely infrared spectroscopy, calorimetry, dielectric spectroscopy, X-ray diffraction, polarized and electron microscopy. The introduction of NPs was found to result in formation of interfacial interactions, an in general moderate elevation of the glass transition temperature and a suppression of the chains fragility/cooperativity. Regarding crystallinity, neither the unfilled PLA nor the PNCs were found to crystallize during cooling from the melt state, whereas all samples crystallize upon heating (cold crystallization), suggesting that the initially slow crystallization and poor nucleation of the used PLA was not improved. The degree of crystallinity upon the addition of NP is also suppressed. Surprisingly, severely more active nuclei were recorded in the PNCs. This is interpreted in terms of the indirect effect of slowing down of the chains' diffusion related to the NP-polymer interaction. This results in slower crystals' growing around more PLA-nuclei in PNCs as compared to the unfilled matrix, within which the antagonistic crystal growing is faster and dominant around less nuclei. This is also manifested by altered crystals structuring in terms of crystals with smaller size and lower density. Regarding local dynamics, the local β relaxation screening the dipolar motions arising from the crankshaft motion of the backbone $-C=O$ was recorded to follow, on the one hand, the formation of interfacial interactions via the suppression of its strength and, on the other hand, to be sensitive to large scale phase changes (glassy to rubbery). Finally, an additional relaxation process was recorded in the highly loaded PNCs and assigned to modified PLA mobility.

Keywords Polylactide · Nanoparticles · Interfacial interactions · Crystallization · Molecular mobility

Introduction

A basic motivation that drives materials' science is the improvement of desired properties, furthermore, the creation of new ones. This is due to the continuously evolving needs for multifunctional materials-systems aiming at gradually more specific applications. A further option is the development of composite materials based on polymers [1], whereas during the last decades, polymer nanocomposites (PNCs) have attracted the main interest [2]. The latter arises from the tremendous improvements recorded for desired properties and performance (e.g., mechanical) with only small amounts of nanoscale fillers [3] as compared to conventional macro-/micro- composites [4, 5]. Responsible for that is considered the quite large surface to volume ratio and aspect ratio of nanofillers. On our days, there has been

✉ Panagiotis A. Klonos
pklonos@central.ntua.gr

✉ Dimitrios N. Bikiaris
dbic@chem.auth.gr

[1] Department of Chemistry, Laboratory of Polymer Chemistry and Technology, Aristotle University of Thessaloniki, 541 24 Thessaloniki, Greece

[2] Department of Physics, National Technical University of Athens, Zografou Campus, 157 80, Athens, Greece

[3] Department of Physics, Aristotle University of Thessaloniki, 541 24 Thessaloniki, Greece

created another frame for materials science, that of green and circular economy [6], which has turned the attention toward biobased, non-toxic and renewable/recyclable polymers. Polylactide, or else, poly(lactic acid) belongs to the latter category, thus, it has already attracted a great amount of interest, for example, from academia and biochemistry [7] to industry (packaging, 3D-printing) [8–10].

PLA [11–14] belongs to the class of aliphatic polyesters, it is thermoplastic and can be both amorphous and semicrystalline. Despite its sustainable character that sets PLA an alternative for replacing the traditional petrochemicals, in general, neat PLAs demonstrate quite poor mechanical performance [13, 15]. Obviously, this can be overcome by manipulating the polymer crystallinity in amount, size and quality of the crystals by various thermal treatments [16–18]. The manipulation can be also achieved by properly chosen plasticizing additives and/or reinforcement via introduction of nanofiller particles [13, 18–22]. As expected, the mechanical performance is strongly connected to crystallinity. In particular, for PLA crystallization is rather slow and weak, due to poor nucleation and slow chains diffusion [23–25]. These depend, among others, on the polylactide structure, i.e., the l- to d-lactide ratio and the polymer chain length (molar mass) [13, 19, 26]. Crystal nucleation and growth can be tuned again by different thermal treatments (large/small supercooling, isothermal annealings, etc.) [16, 27–29], being, however, expensive and non-ecofriendly.

The most effective way to manipulate crystallinity and, subsequently, the mechanical [19, 22], permeation [21, 30] or, even, the heat transport [31] performance, seems to be the dispersion to the PLA matrix of nanoparticles. Moreover, there is the possibility to employ nanoparticles of various chemical structures (metal oxides, carbon-based, clays), 1–3-nano-dimension forms (platelets, tubes, spheres) and surface chemistries (pure or modified). Interestingly, the impact of nanofillers on crystallization can be direct, for example, when the fillers act as additional crystallization nuclei, and indirect, for example when the filler 'steal' the positions of endogenic nuclei. We have experimentally shown, in PLA [18, 24, 25, 32, 33] and other polymers (thermoplastics [34, 35] and rubbers [36]), that the effect of nanofillers facilitating nucleation increases when increasing the fillers aspect ratio and the specific surface area, furthermore, when decreasing the strength of the attractive interfacial filler–polymer interactions [34]. Such results have been partly supported by computer simulations [37]. Thus, there has been demonstrated that the same type of filler, for example silicon dioxide spherical nanoparticles (silica) or carbon nanotubes (CNT), are able to impose opposite effects on the crystallization of a semicrystalline polymer (including PLA) [34, 38]. The degree and strength of the interactions between PLA and a filler (e.g., silica) can be evaluated via the degree of disturbance of the ester group

($-C=O$, polar group) vibration [39] due to bonding with a filler surface group (e.g., $-Si-OH$) [18]. Indirectly, the same interfacial interaction can be evaluated via the corresponding suppression in the heat capacity change during glass transition that is generally recorded in the PNCs as compared to the unfilled matrices [40, 41]. Within the described effects, it is crucial to involve the type of nucleation (homogeneous, heterogeneous, endo- or exo-genic) [16, 17] and the polymer chains mobility in terms of diffusivity and cooperativity. The latter two can be assessed by following the glass transition temperature [40], the polymer chains dynamics and fragility [42], via more sophisticated techniques, such as dielectric spectroscopy [40, 41, 43] and rheology [44]. Therefore, to conclude to a definite impact of nanofillers on the performance of a studied PNC, a sum of various parameters should be followed, namely from the macro- to nano-scale.

In this context of semicrystalline PNCs, herein, we attempt to check the impact of fumed silica nanoparticles at a relatively wide range of loadings (2–10 mass%) on the crystallization, glass transition and molecular dynamics of a specific PLA, namely of moderate molar mass and containing ~ 96 l- and ~ 4 d-lactic isomers. To that aim, a battery of complementary techniques is employed here, as follows. For this structure-mobility relationship investigation we employed Fourier transform infrared (FTIR) spectroscopy, conventional differential scanning calorimetry (DSC), polarized light microscopy (PLM), X-ray diffraction (XRD), scanning electron microscopy (SEM) and broadband dielectric spectroscopy (BDS) [43, 45]. Moreover, we compare the results by the present study with those for similar or different PLA (e.g., of 100% l-lactide and severely longer chains) reinforced by the same or different silicas [18, 38] as well as various other nano-inclusions [24, 25, 33].

Materials and experimental methods

Materials

PLA with ~ 96% l- and ~ 4% d-lactide (else called PLDLA), and molecular weight of $M_w = 75$ kg mol^{-1}, under the trade name Ingeo™ Biopolymer 3052D, was kindly supplied by Plastika Kritis S.A. (Iraklion, Greece). Fumed silica (SiO_2) nanoparticles Aerosil® 200 with specific surface area of 200 m^2 g^{-1} and initial nanoparticle size < 15 nm were supplied by Evonik, Essen, Germany. All other used solvents and reagents were of analytical grade and purchased from Sigma Aldrich (USA).

Preparation of polymer PNCs

A series of PLA/silica PNC films of different silica loading, namely 2, 4, 6, 8 and 10 mass%, were prepared using

the solvent casting method. Briefly, dispersions of a final concentration 10% w/v (3 g of PLA and nanofiller/30 mL solvent) were formed, by first dissolving PLA in chloroform and then by dispersing the appropriate amount of nanosilica using a sonicator probe. The mixtures were continuously stirred for 2 h in a fume hood and were then poured on a glass plate. The obtained PLA/silica films were dried at room temperature, RT, for 24 h and, afterward, for 8 h under vacuum to reach total solvent evaporation.

Characterization methods

FTIR spectra were obtained using a Perkin-Elmer FTIR spectrometer, model Spectrum One. The materials were in the form of thin films with thickness of approximately 15 μm and in the amorphous state. The spectra were obtained in absorbance mode and in the spectral region of 400–4.000 cm^{-1} using a resolution of 4 cm^{-1} and 64 co-added scans.

Conventional calorimetry (DSC) was employed to assess the polymer's thermal transitions. For that, a TA Q200 series DSC instrument (TA, USA), combined with a liquid nitrogen control system, calibrated with sapphires for heat capacity and indium for temperature and enthalpy, was used. The measurements were performed in high purity nitrogen atmosphere, on samples of ~7 mg in mass closed in Tzero aluminum pans of TA and in the temperature range from −10 to 200 °C. The selected measurement protocols are described below and are schematically shown in Fig. 1a for more clarity. Upon erasing of any thermal history (*scan 1*) by a first heating scan at 200 °C, (*scan 2*) the samples were subjected to cooling from the melt state at 10 K min^{-1} and (*scan 3*) at the highest achievable rates, i.e., ≥ 100 K min^{-1} at the temperature range of expected the crystallization (Fig. 1b, 'jump' command). Subsequently, the samples were heated at 10 K min^{-1} up to 200 °C. Since neither of the

samples could crystallize during cooling a final scan was performed (*scan 4*) on the super-cooled samples, involving heating at 10 K min^{-1} from − 10 to 120 °C, i.e., above glass transition and below melting, isothermal stay there until completion of cold crystallization (10 min being found sufficient), subsequent cooling to − 10 °C and, finally, heating of the semicrystalline sample up to 200 °C.

The semicrystalline morphology of the samples was examined employing PLM, by means of a Nikon Optiphot-1 polarizing microscope equipped with a Linkam THMS 600 heated stage, a Linkam TP91 control unit and a Jenoptik ProgRes GRYPHAX® NAOS 20mp microscope camera, during cold crystallization at the 120 °C beginning from the amorphous state (similarly to *scan 4* in DSC).

To assess any effects on the structure of the PLA crystals, XRD at RT was employed on samples suffered cold crystallization at 120 °C (again beginning from the amorphous state, as in the DSC *scan 4*). The XRD spectra were recorded by means of a MiniFlex II XRD system (Rigaku Co., Japan), with Cu Ka radiation ($\lambda = 0.154$ nm), over the 2θ range from 5° to 50° with a scanning rate of 1° min^{-1}.

The surface morphology of the prepared materials was determined by SEM/Energy-Dispersive X-ray spectroscopy (SEM/EDS) using the JEOL JMS-840 system (JEOL USA Inc., Peabody MA, USA) operated at 5 kV.

Finally, BDS was employed to study the molecular mobility on all samples in the initially amorphous state. Measurements were performed by means of a Novocontrol BDS setup (Novocontrol GmbH, Germany), in nitrogen gas flow atmosphere on samples in the form of sandwich-like capacitor. In particular, pieces of the samples were placed between finely polished brash disk-electrodes, melted at 200–210 °C using thin silica spacers (~ 100 μm) to keep the distance between the electrodes constant and prevent electrical contact. Based on the results by DSC, this process produces amorphous samples. The diameter of the upper electrode
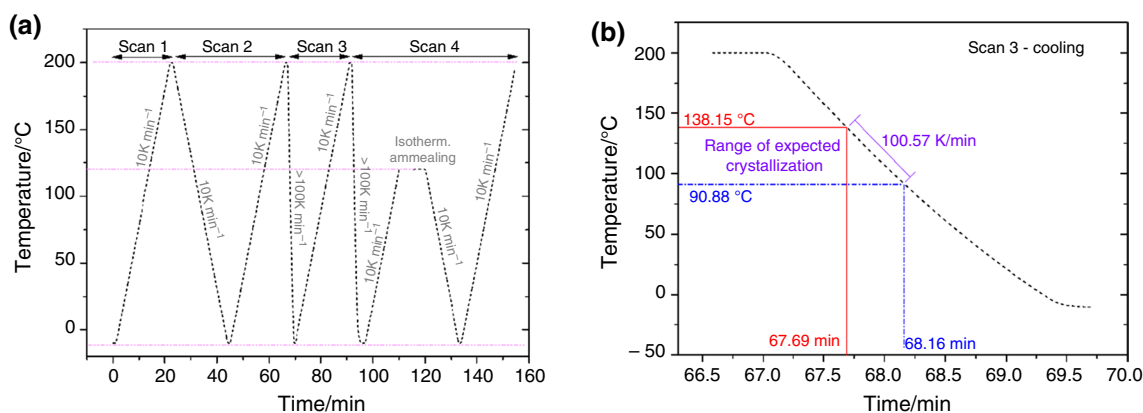
Fig. 1 **a** The time–temperature profiles during *scans 1–4* performed for the DSC measurements. **b** The time–temperature profile of the relatively fast cooling during scan 3. A rough estimation of the cooling rate is supplied at the temperature range of PLA's crystallization

was fixed to 14 mm. The complex dielectric permittivity, $\varepsilon^*(f,T) = \varepsilon'(f,T) - i \cdot \varepsilon''(f,T)$, was recorded isothermally as a function of frequency in the range from 10^{-1} to 10^6 Hz and in the temperature range between -150 and 120 °C, upon heating at steps of 5 and 10 K. For the selected PNC with 10% silica, BDS scans were recorded also upon subjecting the sample to cold crystallization at 120 °C (as in DSC *scan 4*).

Results and discussion

### Structure and polymer-filler interactions

In Fig. 2a we present results by FTIR for all samples, neat PLA and the corresponding PNCs, data for initial silica being also including for complicity. The results are in accordance with findings from the literature on PLA [18, 25, 33]. The molecular origins of the main recorded peaks (methyls, carbonyls of PLA) are described on the plot.

Following other basic studies, on PLA [18] and different polymers [39], we focus on carbonyl site (–C=O) [46] which is located within the wavenumber range from ~1600 to 1850 cm^{-1} in Fig. 2a. Since this group is the most polar site of PLA, it is most probable to be involved within any interfacial (or inter chain interactions). On the other hand, silicas are characterized by large numbers and surface density of surface silanols (–Si–OH) [47], the hydroxyls (–OH) of which are expected to directly interact with PLA, most probably via formation of hydrogen bonds with the carbonyls.

In Fig. 2b, we have reproduced the results from Fig. 2a, focused on the region of the stretching/vibration of the PLA carbonyls [48] and performed baseline corrections and shape normalizations to each peak maxima [18, 39]. The said peak demonstrates a broadening in PNCs and a systematic increasing of the contribution at the lower wavenumbers side with the increasing of silica loading (vertical red arrow in Fig. 2b). Such effects, of the same [18, 39] as well as other polar groups [34], have been interpreted in terms of increasing of the bound (disturbed) group fraction at the expenses of the free (unbound) ones. More precisely, when the corresponding FTIR carbonyls peak is located at high wavenumbers, the vibration is expected to be more extensive or/and faster and, thus, more energy consuming. This occurs in the case of free –C=O. On the other hand, when some of the –C=O are implemented within direct interactions with some of the surface –OH of silica, the freedom of vibration for –C=O is suppressed. This is recorded in FTIR as an increasing of contributions toward lower wavenumbers (less energy consuming). The latter non-free carbonyls are considered 'bound' [39]. We recall that the shown FTIR spectra have been recorded from samples in the amorphous state and, therefore, any affects recorded on the disturbance of the PLA carbonyls are due to the abovementioned interfacial interactions.

From the analysis of the complex peaks of Fig. 2b in terms of mathematical models, namely fitting Gaussians for the free and bound contributions [39] (not shown), we may estimate the area of the bound carbonyls contribution, A_{bound}. When comparing the latter with the total area for carbonyls (bound and free), A_{TOTAL}, [39] a first approximation on the fraction of bound carbonyls, $X_{FTIR}(\%) = \frac{A_{bound}}{A_{TOTAL}} \times 100$, is gained. The results for X_{FTIR} are shown in the inset to Fig. 2b, demonstrating a continuous increase from 7% (for 2% silica) up to 14% (for 10% silica). The trend is not linear,
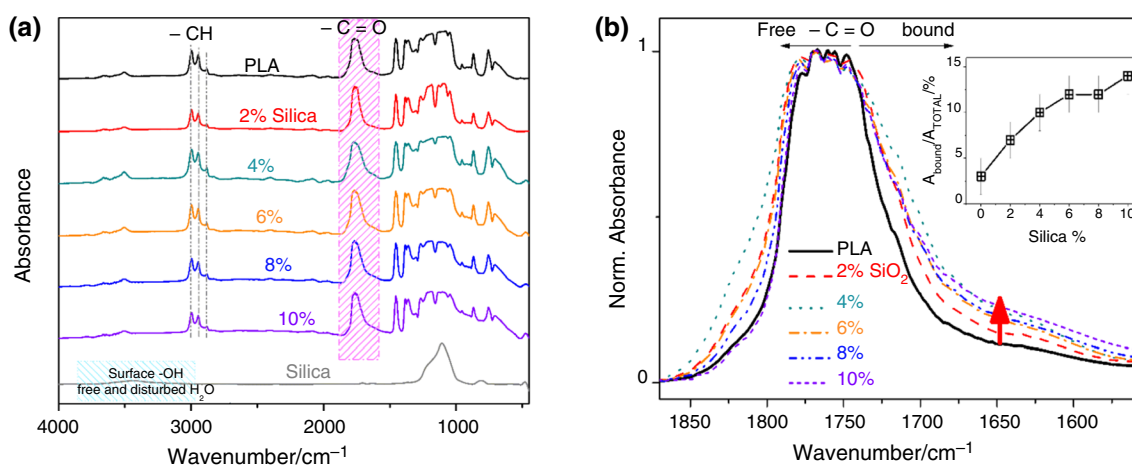
Fig. 2 **a** Comparative FTIR absorbance spectra for PLA and PLA/silica PNCs. Data on initial silica are shown for comparison. **b** The FTIR region of –C=O vibrations, reproduced from **a** however upon shape normalization to the peak maxima. The arrow marks the addi-

tive silica contribution to the smaller wavenumber side of the peak (disturbed/bound carbonyls), whereas the inset shows the estimated fraction of bound carbonyls, X_{FTIR}, against the silica loading (details in the main text)

moreover, the slope decreases with increasing silica. This most probably denotes that the fraction of accessible silica hydroxyls (accessible) surface area for PLA is not analogue to the number of nanoparticles. Quite easily, the effect is rationalized by the expected aggregation of the silica particles for higher contents, despite the solution casting method employed for the preparation of PNCs. Finally, from the employed method of X_{FTIR} calculation, for neat PLA X_{FTIR} is 3% (i.e., $\neq 0$). This suggests, that a number of carbonyls are already 'bound,' possibly due to chain-chain entanglements, if not also due to formation of crystallization nuclei (physical crosslinks) [49], as the samples were already supercooled [17]. Given the relatively high amounts of silica here, X_{FTIR} is low, comparing with previous polylactides [18, 25] as well as other polymers [39] filled with silica. This could be due to the strength of its individual interaction [33] and/or the high chain rigidity [41, 50] of the specific PLA here.

In previous studies on various PNCs [18, 26, 34, 39, 47], X_{FTIR} was directly correlated with the amount of the interfacial rigid amorphous fraction (RAF) [40] obtained by DSC. Such correlation is being attempted in the following.

Glass transition, rigid amorphous fraction and crystallization

In Fig. 3, we present the DSC traces for neat PLA for all performed scans. Therein, PLA exhibits no melt (hot) crystallization, neither by cooling at 10 K min^{-1} (dashed line in Fig. 3a) nor by faster rates (not shown). Eventually, upon conventional cooling, sharp glass transition steps recorded during *scans 1–3* (Fig. 3b) that correspond to amorphous samples. The characteristic temperatures of glass transition, T_g, estimated by the half heat capacity (c_p) change, Δc_p, are 57 °C for *scans 1* and *3* and 56 °C for *scan 2*, i.e., almost identical. The corresponding Δc_p is 0.54–0.55 J g^{-1} K^{-1} for the amorphous PLA. An overshoot is observed during glass transition, again for the amorphous samples, the strength of which is quite large for scan 1 (erasing history scan), moderate for scan 2 (upon moderate cooling rate) and less for scan 3 (upon faster cooling). The overshoot is related to the structural relaxation [51, 52] and connected to high freedom of chain motions; therefore, the recorded results are expected in terms of enhancement of the overshoot with increasing the time periods of the samples stay at temperatures closely below T_g [53, 54]. The overshoot vanishes in the case of semicrystalline samples (*scan 4*, Figure 3b) due to additional and severe constraints induced to the polymer chains mobility [53].

Coming back to *scans 1–3*, PLA exhibits strong cold crystallization during heating, with the exothermal peaks maxima (minima in Fig. 3), T_{cc}, being between 103 and 107 °C. The effect suggests not significant effect by thermal history on the crystallization (nucleation) of the specific PLA. The same connection between absence of hot crystallization and presence of cold crystallization has been observed before in similar PLA (namely PLDLA with ~4% d-lactide and M_w of 63 kg mol^{-1} [25]) with, however, weaker cold crystallization. The absence of hot crystallization has been connected to poor nucleation due to the said d-lactide content in combination also with the moderate M_w. For example, in the case of PLA with 0% d-lactide (i.e., PLLA) and higher M_w (e.g., 700 kg mol^{-1} [32]) the polymer easily crystallizes during a conventional
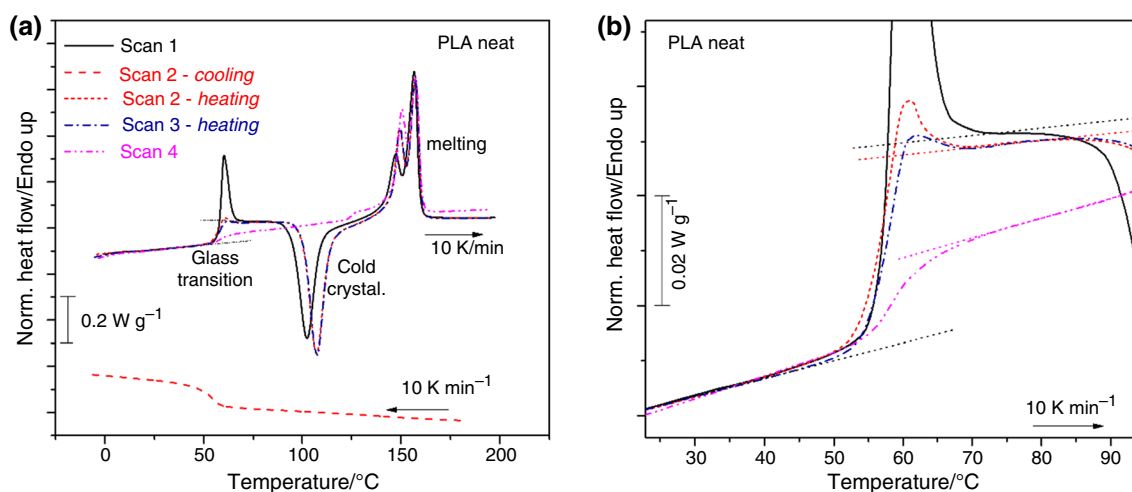
Fig. 3 **a** Comparative heating/cooling DSC curves for the unfilled neat PLA (matrix) for the four thermal protocols employed in this work (the results by fast cooling at > 100 K min^{-1} have been also included). **b** Shows the same results with focus on the glass transi-

tion region during heating. The added dotted lines in **b** represent the baselines before and upon glass transition. The heat flow curves are shown upon normalization to each sample mass

cooling from the melt state. On the contrary, PLA consisting of uniquely d-form (i.e., PDLA) is completely amorphous [26]. The crystalline fraction, CF, or else called degree of crystallinity, can be estimated by comparing (Eq. 1) the enthalpy change during cold crystallization, ΔH_{cc}, with the theoretical value for the enthalpy change of a fully crystalline PLA, taken usually as 93 J g^{-1} from the work by Fischer et al. [55]. Prior to that, the recorded ΔH_{cc} should be normalized ($\Delta H_{cc,n}$) to the polymer mass, $w_{polymer}$.

$$CF_{cc} = \frac{\Delta H_{cc}}{w_{polymer} \cdot \Delta H_{100\%}^{PLA}} = \frac{\Delta H_{cc,n}}{\Delta H_{100\%}^{PLA}} \tag{1}$$

Here, $\Delta H_{cc,n}$ is 34–35 J g^{-1} and CF_{cc} equals 0.37–0.38 for neat PLA and *scans 2–3*. It should be noted, for the sake of completeness, that more recently compared to

Fischer et al., Righetti et al. [29] reported larger values for enthalpy of melting of 100% crystalline poly(L-lactic acid), namely 107 and 143 J g^{-1}, for α- and α'-crystal-forms, respectively.

At higher temperatures in Fig. 3a, the recorded endothermal peaks correspond to the melting of crystals. Melting is structured as 'double' peak, expected for the specific type of PLA [25, 33], and the characteristic peak temperatures are $T_{m1} = 149$ °C and $T_{m2} = 157$ °C.

Coming to *scan 4*, when subjecting the samples to cold crystallization from RT to 120 °C and staying isothermally there, the glass transition migrates to $T_g = 59$ °C and becomes wider (Fig. 3b) and its strength (Δc_p) drops to 0.24 J g^{-1} K^{-1}, since a large part of the polymer chains from the amorphous state does contribute to the glass transition in the semicrystalline state.
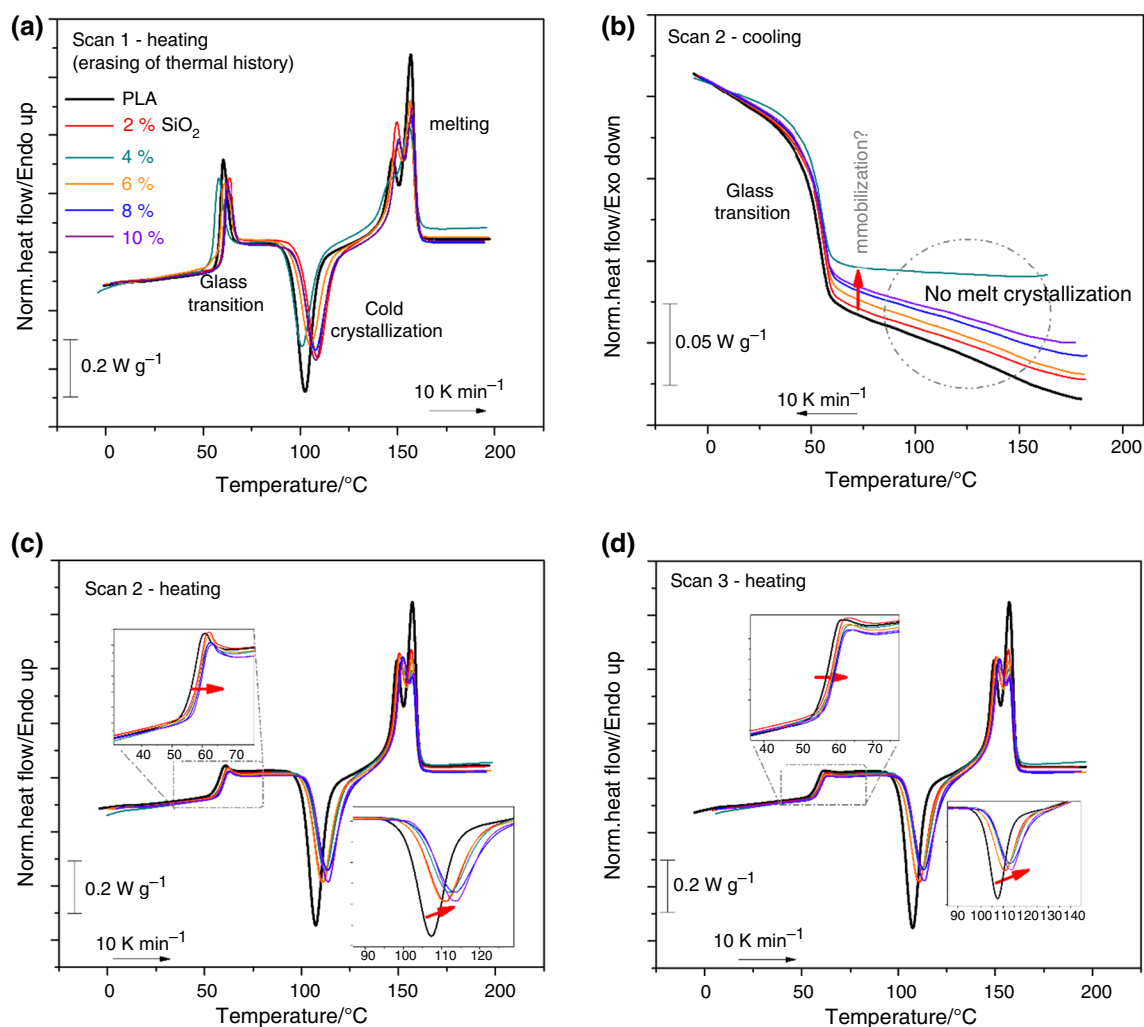
Fig. 4 **a** Comparative DSC curves for PLA and all silica-filled PNCs during **a** heating of scan 1, **b**, **c** cooling and heating of scan 2 and **d** heating of scan 3. The shown heat flow values (i.e., in mW) have been normalized to the sample mass (i.e., in W g^{-1}). The added arrows mark the effects imposed by the silica addition

We may discuss now the situation in the PNCs, particularly, the effects imposed by the silica addition on PLA. In Fig. 4, the overall raw DSC data for *scans 1–3* are shown in the form of comparative heating and cooling traces. In addition, the corresponding results by *scan 4* are shown in Fig. 5.

The main thermal transitions observed above for PLA, are also recorded in the PNCs with mainly quantitative changes. One of the most important results by this work refers to hot/melt crystallization. In Fig. 4b, none of the PNCs exhibits melt crystallization peaks. In addition to that, in Fig. 4c, d, all PNCs exhibit retarded and weaker cold crystallizations as compared to that of neat PLA. These recordings are strong indications that the employed nanosilicas do not facilitate crystallization, neither in terms of nucleation nor in easier chains diffusion. Looking back in previous works on PLA/silica PNCs, there can be found cases of the same and other silicas facilitating the melt crystallization of PLLA [18, 38] as well as the cold crystallization of PLDLA [25].

To more easily follow the aspects on crystallization as well as glass transition and melting, all data by DSC were evaluated in terms of characteristic values (temperatures, enthalpy and heat capacity changes) and the latter are presented as silica content dependences in Figs. 6, 7and8.

First, we focus on the glass transition. In the amorphous state, $\Delta c_{p,n}$, the measure of the mobile amorphous fraction (MAF) [56], is lower in the PNCs, as shown in Fig. 6a. This effect has been interpreted in various works on PNCs [40, 41, 56–59] to be due to the immobilization of polymer chains onto the filler's surface when attractive interfacial interactions are formed. The presence of the fillers with attractive interactions may result in general in hindering of chains diffusion, recorded as an elevation of the T_g [40, 41, 56, 60]. This is also true here in Fig. 6a, wherein the T_g of the PNCs elevates by 1–2 K. The changes in both Δc_p and T_g are non-monotonic with the silica loading. Similar trends are discussed in the following on the characteristic crystallization. The effects suggest that most probably the nanosilicas are better dispersed in the PLA
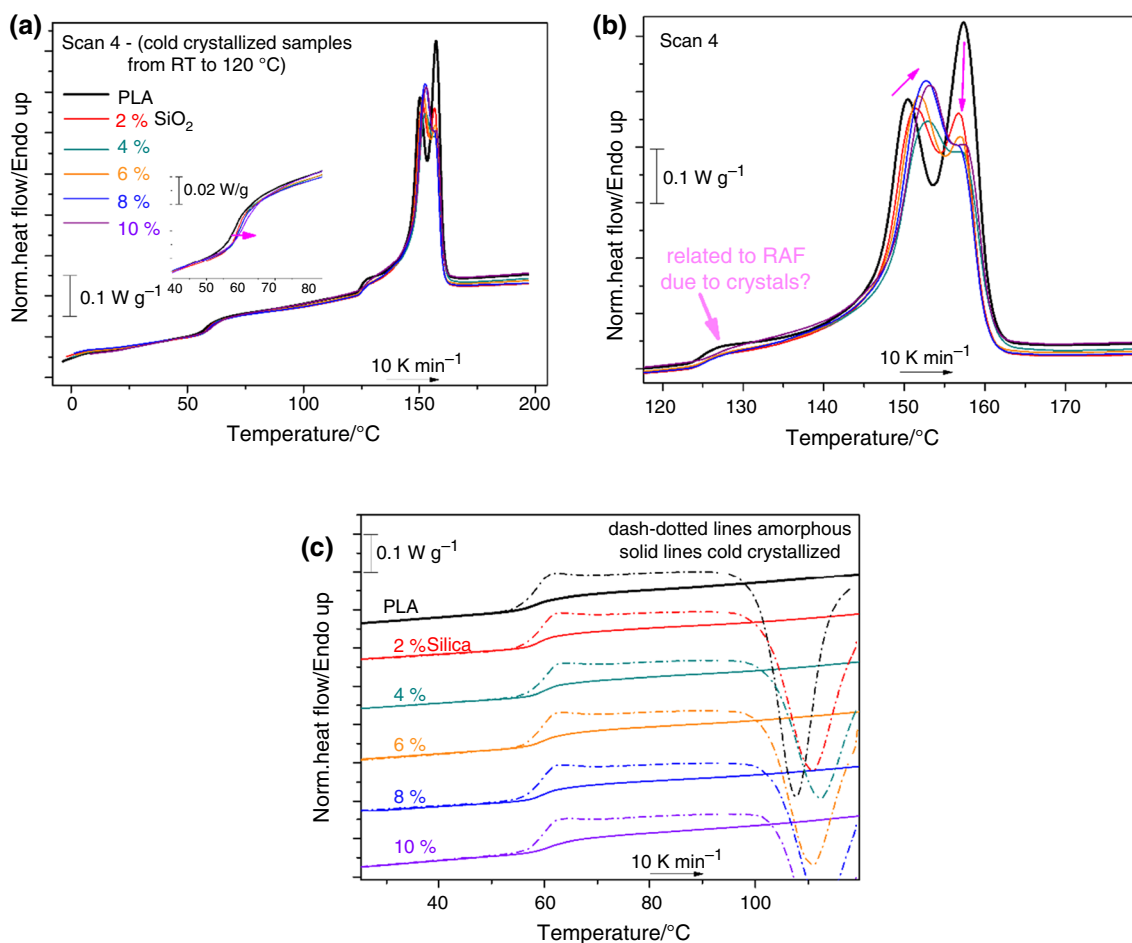
Fig. 5 Comparative DSC traces during *scan 4* for all samples during **a** heating in the overall temperature range, **b** focusing on the melting and pre-melting effects range, and **c** in the glass transition region. In **c**, the data by *scan 4* (solid lines, semicrystalline state) are directly compared with those by scan 3 (dash-dotted lines, amorphous state). The shown heat flow curves have been normalized to the sample mass
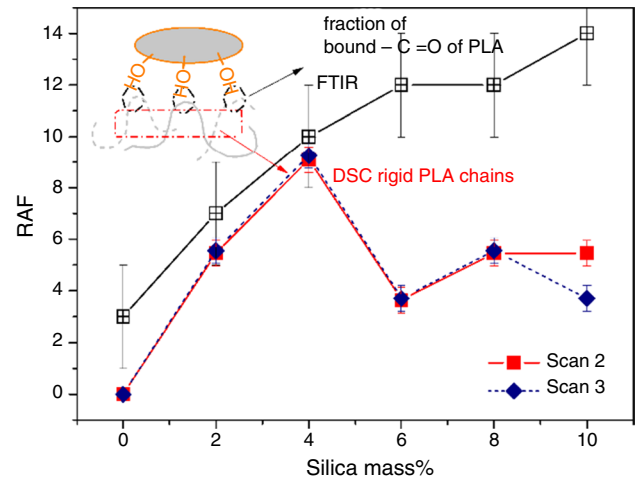
(a)

(b)
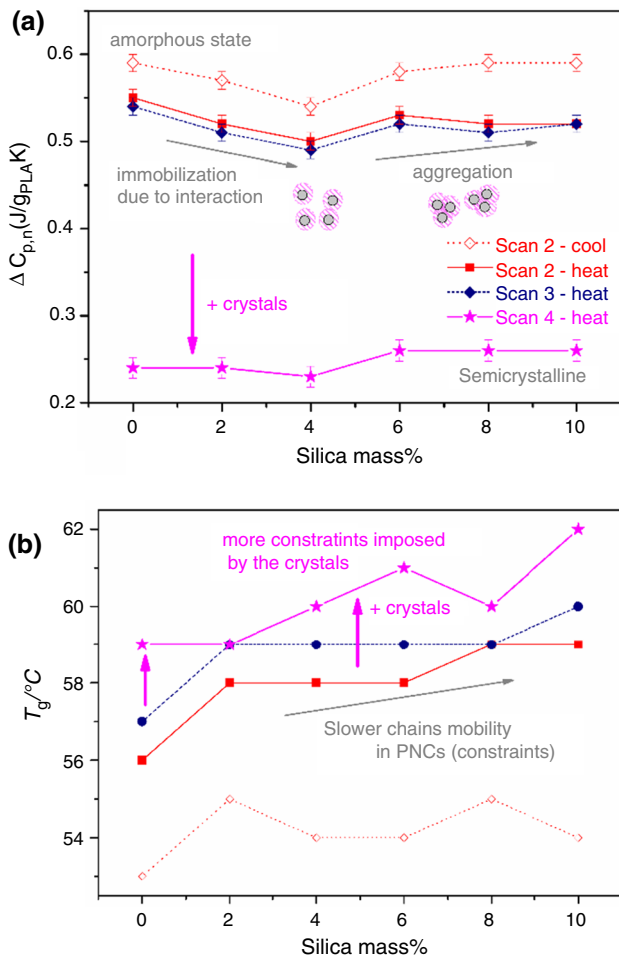
Fig. 6 Evaluation of the overall DSC data of glass transition, in terms of the silica loading dependences of **a** the normalized heat capacity change and **b** the glass transition temperature
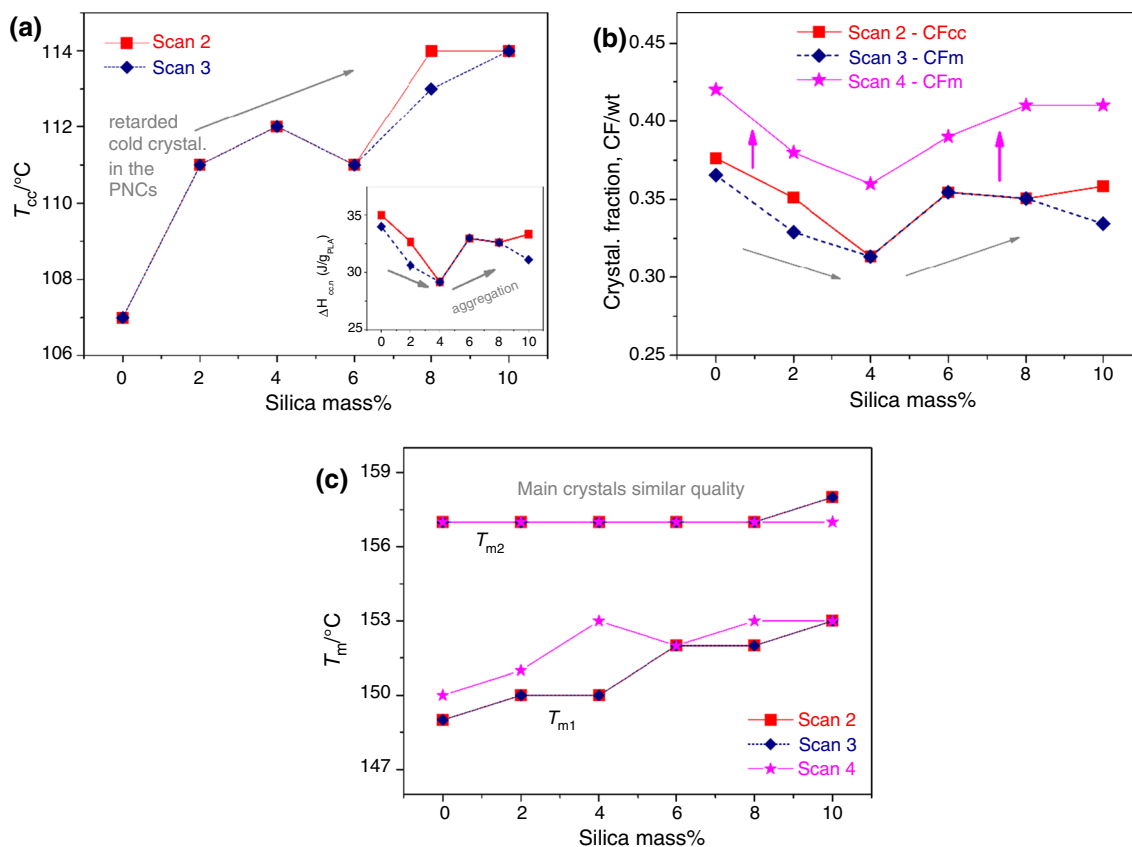

Fig. 7 The silica loading dependences of the estimated amount of the rigid amorphous fraction, or else of the interfacial PLA chains, in the case of the amorphous samples from *scans 2 and 3*. The data on RAF are compared with those by X_{FTIR}. The added scheme describes the different physical origins between FTIR and DSC on estimating the silica-PLA interfacial polymer fraction

matrix at low contents (2 and 4 mass%), whereas aggregation has taken place for larger loadings [56]. We attempted to check that by SEM (results shown in Figure S1 in Supplementary Material), nevertheless, unsuccessfully, mainly due to the need for extremely better resolution.

Both the Δc_p and T_g do not show tremendous changes in the PNCs, which suggests weak interfacial interactions. To evaluate this by DSC, we may employ a 'two-phase' model [40, 57, 61] for our PNCs in the amorphous state (*scans 2 and 3*), considering that the polymer consists of mobile and rigid (interfacial) amorphous fractions, MAF and RAF, respectively, with 'RAF+MAF=100%.' The MAF is that contributing to the glass transition. Thus, we may estimate RAF via Eq. 2.

$$\text{RAF}(\%) = (1 - \text{MAF}) \cdot 100 = (1 - \frac{\Delta c_{p,n}^{PNC}}{\Delta c_{p,n}^{MATRIX}}) \cdot 100 \quad (2)$$

The results on RAF are shown in Fig. 7. Since RAF can be used as a measure of the polymer-silica interaction,

we may compare it with the more direct result by FTIR, X_{FTIR}. Keeping in mind the *in principle* different routes of estimation (inset scheme to Fig. 7), we interestingly come in front of quite similar values of RAF and X_{FTIR}, at least for the lower silica loadings. The low RAF values here, as compared to previous works of PNCs with attractive polymer-particles, are confirmed by DSC. It is also worth to recall some results from the literature on PNCs, within which the increase in T_g is directly correlated with the increase in the interfacial RAF [57, 58, 61, 62], which fits with our case here and the barely increased T_g.

From another point of view, another indirect evidence for the weak interfacial interactions and their low effect on molecular mobility, can be extracted by the recorded preservation of the overshoot during the glass transition in the amorphous PNCs (insets to Fig. 4c, d). The strong overshoot is indicative of the preservation of the bulk-like freedom of motions here. In previous cases of PNCs with quite more strong interfacial interactions the overshoot is minimized or, even, disappears [40, 41, 63].

Coming to the semicrystalline PNCs, we follow in Fig. 8a an increasing trend of T_{cc} with the silica loading, with a discontinuity of the increase for 6% silica. At the same time the cold crystallization enthalpy changes (inset to Fig. 8a); consequently, CF_{cc} in Fig. 8b decreases in the PNCs. The results for CF_{cc} are almost identical with CF estimated via the enthalpy of melting (CF_m, not shown). The lower CF_{cc} value is recorded at 4% silica, while CF_{cc} increases for the higher silica loadings. As discussed above with Δc_p and RAF, the non-monotonic changes should be

Fig. 8 Evaluation of the overall DSC data of crystallization and melting, in terms of the silica loading dependences of (**a** and inset) the cold crystallization temperature and enthalpy change, T_{cc} and $\Delta H_{cc,n}$, respectively, **b** the amount of crystalline fractions, by cold crystallization, CF_{cc}, and melting, CF_m, and (**c**) T_m

due to differences in the particle's distributions throughout the polymer matrix.

When the polymer is subjected to cold crystallization (*scan 4*), upon the subsequent heating (Fig. 5a), CF_m was estimated and the data are included in Fig. 8b. The trend is qualitatively similar to those of CF_{cc}, while CF_m is larger by about 0.05 for *scan 4*.

Regarding melting, the view of double melting peaks observed in neat PLA is kept in the PNCs (Figs. 4c, d and 5b) and this is independent from the employed thermal treatments. The higher temperature peak ($T_{m2} = 157$ °C) is unchanged between all cases in Fig. 8c. The lower temperature peak (T_{m1}) migrates toward higher temperatures at the addition of silica in Fig. 8c. Interestingly, T_{m1} is almost identical upon *scans 2* and *3*, whereas it is elevated upon *scan 4*. We could conclude that while T_{m2} represents the main and more stable crystals of PLA, T_{m1} originates on the melting of less stable crystals and, most probably, of lower quality/density.

Recalling previous knowledge, PLA exhibits crystal polymorphism [16, 29, 64], for example, α and α'-type crystals. In the case of melt crystallization at temperatures greater

than 120 °C, the orthorhombic α-type crystals dominate, with an equilibrium melting temperature of around 220 °C. On the other hand, isothermal crystallization from the melt at temperatures lower than 120 °C or isothermal annealing at temperatures higher than T_g leads mainly to the formation of α'-crystals characterized by lesser order. The dependence of PLA's crystallization behavior from the annealing temperatures, time periods, the heating rate and the l-/d-isomers content has been systematically investigated in previous works [27, 29, 65]. In our case, we expect the domination of α'-type crystals, thus, low level of ordering which is reflected on the discussed effects on T_{m1}. The effect of silica on the increasing of T_{m1} should be indirect, as the crystals seem to grow away from the nanoparticles (not nucleating agents, opposite to previous cases [32, 36, 66]); however, the origins seem not straightforward based only on the calorimetric recordings.

Regarding DSC, a last but not least point refers to Fig. 5a, b. Therein, during heating at temperatures just prior to the melting peaks, a step-like event is observed for all samples. The step is clear upon *scan 4*, compared to *scans 1–3*, due to the absence of the cold crystallization exotherm. Such step

has been observed before in semicrystalline polymers (e.g., isotactic polystyrene [67] and polylactide [68]) by conventional as well as temperature modulation DSC. This transition has been proposed to originate on the vitrification of rigid amorphous chains located around the polymer crystals ($RAF_{crystal}$) [67, 68].

Semicrystalline morphology and crystal structure

To visualize the situation around the crystallization of PLA and the PLA/silica PNCs, PLM was employed, in particular,

imitating the thermal treatment of *scan 4* in DSC. In Fig. 9, the PLM micrographs of all samples are shown during their cold crystallization from the initially amorphous state at RT, heating to 120 °C and isothermal stay there until completion of crystallization.

Surprisingly, all PNCs seem to crystallize faster (left side of Fig. 9) and fill the sample volume with more crystals (right side of Fig. 9) as compared to neat PLA. At first thought, this seems completely opposite to the calorimetric recordings, as the recorded semicrystalline view of our PNCs resembles previous cases of PNCs were in the fillers
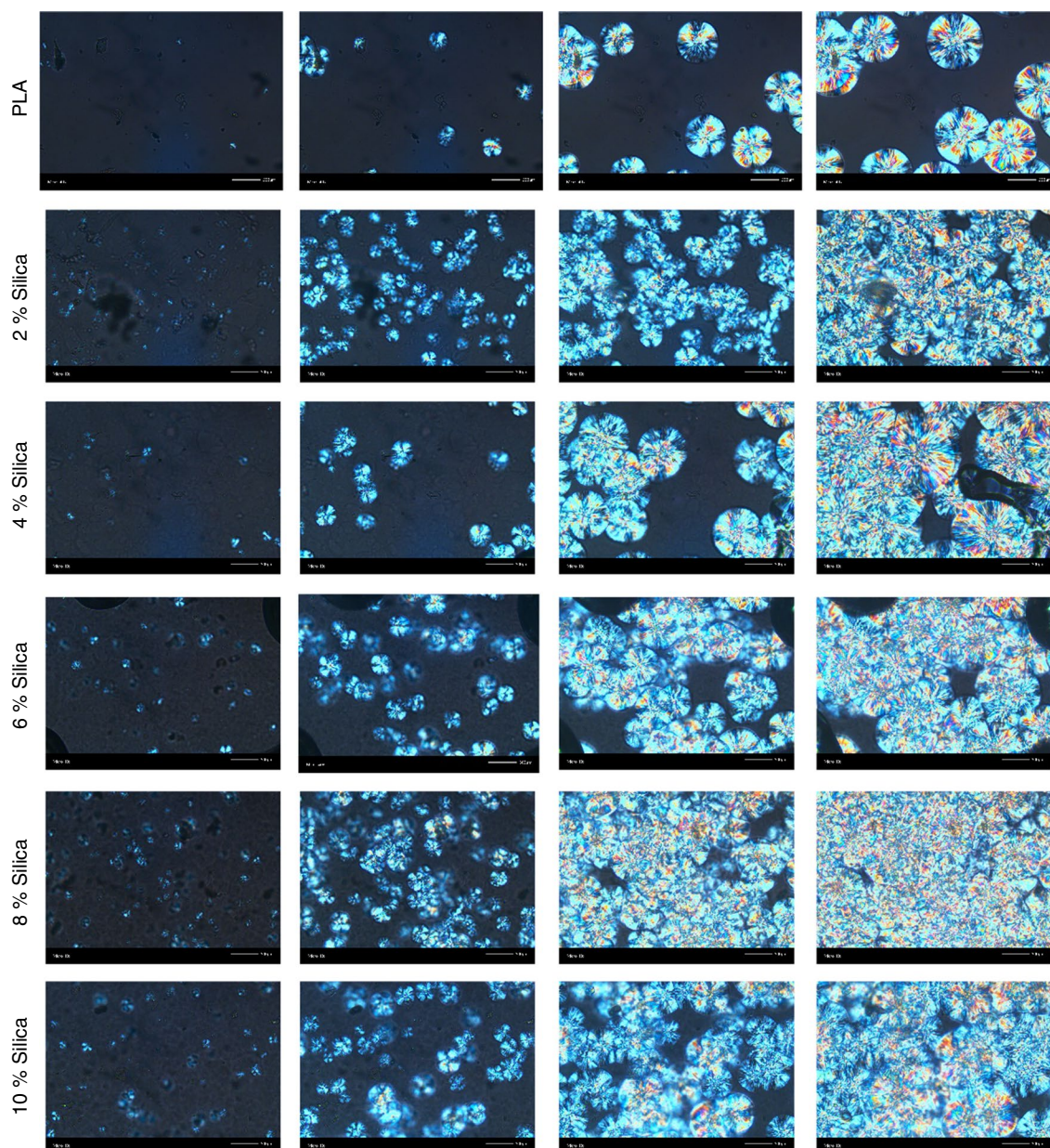
Fig. 9 PLM micrographs during cold crystallization of all initially amorphous (supercooled) samples at 120 °C. The scale bars correspond to 50 μm

act as crystallization agents and the crystals are developed also around the particles [18, 20, 25, 33]. However, in those previous cases, the DSC results showed acceleration and enhancement of both the melt and cold crystallization at the presence of the nanofillers, that is opposite to our case. Thus, we are in front of an apparent although serious discrepancy between calorimetry and PLM.

From the PLM data we were able to make a rough estimation of the spherulitic growth rate, $G(t)$. This was done during the crystallization steps (not isothermally as usually) by following the free growth of a minimum of three spherulites before they impinged on one another. Then, the radius of each spherulite was measured and plotted as a function of measurement time. From this plotting, we estimated the slope, which represents G. G was found ~ 60 μm min^{-1} for unfilled PLA, while drops almost systematically with the silica addition, from 52 down to 41 μm min^{-1}. Please note, that the uncertainty in δG is rather high, $\delta G \sim 20$ μm min^{-1}.

One way to rationalize the overall results and explain the discrepancy between calorimetry and PLM can be the following. Prior to the cold crystallization of neat PLA, there have been created large numbers of crystal nuclei, due to the strong cooling involved. During the cold crystallization, upon heating at temperatures closely above T_g, only a fraction of the overall existing nuclei seem to be active, or in other words, only some of the nuclei favor a fast crystallization. These initial crystals seem to grow fast and preclude the formation of secondary crystals. This way, we expect the formation of low number of crystals with, however, large size and potentially high density or thick lamellae packing. For the PNCs, we recall the slightly elevated T_g, thus, an expected deceleration of molecular mobility, which actually seems to have the key-role on the following crystallization. In the presence of nanofillers, PLA seems to also form large numbers of nuclei with, according to PLM, more

active nuclei. It is possible that due to the retarded chains diffusion there is no antagonism between initial (faster) and secondary (slower) crystals and mainly the 'slower' ones survive. For the PNCs, to rationalize the lower CF_{cc} values recorded in DSC (Fig. 8b) along with the 'contrary' larger number of crystals observed in PLM (Fig. 9), we could only suppose that the many crystals formed should be of quite lower quality/density. This is not supported by the melting ($T_{m1,2}$) from DSC. To more firmly check the situation on the crystals structuring we employed XRD.

Figure 10 shows the corresponding XRD results on PLA and its PNCs that had previously suffered the same thermal protocol to those of *scan 4* in DSC and PLM.

The results by XRD in Fig. 10a reveal mainly the same number of crystalline peaks between the unfilled matrix and the PNCs. Upon analysis of the XRD spectra (examples being shown in Figure S2 in Supplementary Material), we could estimate the crystalline fraction of the samples by comparing the areas of the crystalline peaks, A_{cryst}, with the total area of the spectra (amorphous halos and crystalline peaks), A_{TOTAL}, according to Eq. 3.

$$CF_{XRD}(\%) = \frac{A_{cryst}}{A_{TOTAL}} \cdot 100 \tag{3}$$

The CF_{XRD} values against the silica loading are shown in Fig. 10b along with those by CF_m by DSC *scan 4*. The results by the two techniques are quantitatively different, with CF_{XRD} being lesser by 10–15% than CF_m, however, the silica loading trends are quite similar.

The most important finding by XRD is a migration of the diffraction peaks toward higher 2θ positions in the PNCs, with the exception of PLA + 10% silica. Actually, the migration is weak for 2 and 4% silica and stronger for 6 and 8% silica. The migration toward higher 2θ can be
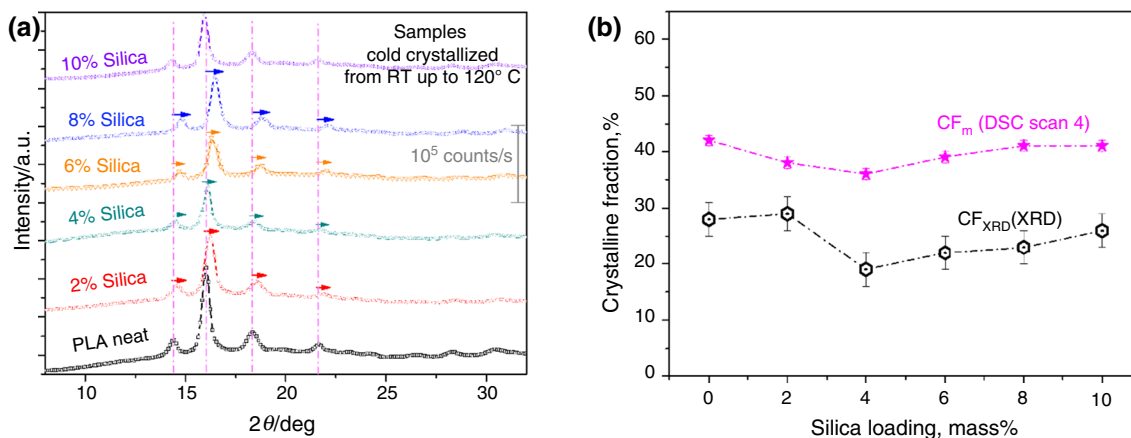
Fig. 10 **a** XRD spectra for all samples upon cold crystallization. **b** Estimated crystalline fraction upon analysis of the XRD spectra, CF_{XRD}, the results being compared with CF_m from DSC of *scan 4*

understood as formation of thinner crystalline lamellae [33], thus, worse crystal density and lower ordering level. This comes to support the scenario described above, at least partly, since one PNC shows similar XRD positions to those of neat PLA.

At this point, we recall some results from the literature. In previous cases of PNCs, based on PLA [18, 20, 24, 25, 33] and other polyesters [34, 69], with the fillers (including silica) acting as crystallization nuclei, the crystallization (melt and cold) was accelerated and enhanced in DSC. Additionally, the corresponding XRD diffraction peaks migrated toward lower 2θ, being interpreted therein as formation of more dense crystals in the PNCs. The latter effects on crystal structuring were found to correlate in PLM with both smaller and larger spherulites in the PNCs as compared to each unfilled matrix.

Local and segmental molecular mobility

Molecular mobility is investigated by BDS, in particular via effects on the imaginary part of dielectric permittivity, ε'', which expresses the dielectric losses [43]. The initial recordings, namely isothermal $\varepsilon''(f)$ spectra were recorded at various temperatures from $-150\,°C$ up to $120\,°C$ on initially amorphous samples, intending to illuminate the direct filler-effects. These overall data can be found in Figure S3 in Supplementary Material. The molecular dipolar relaxations are followed in these data as 'peaks' of the $\varepsilon''(f)$, the maxima of which are located at gradually increasing frequencies, f_{max}, with increasing of the temperature (dynamics). For the sake of simplicity, in the main article we show representative results in Fig. 11, in the form of comparatives for all samples.

Two types of relaxations are clearly recorded within the studied temperature range. At the lower temperatures, from about -100 to $-20\,°C$ (glassy polymer state), the local β
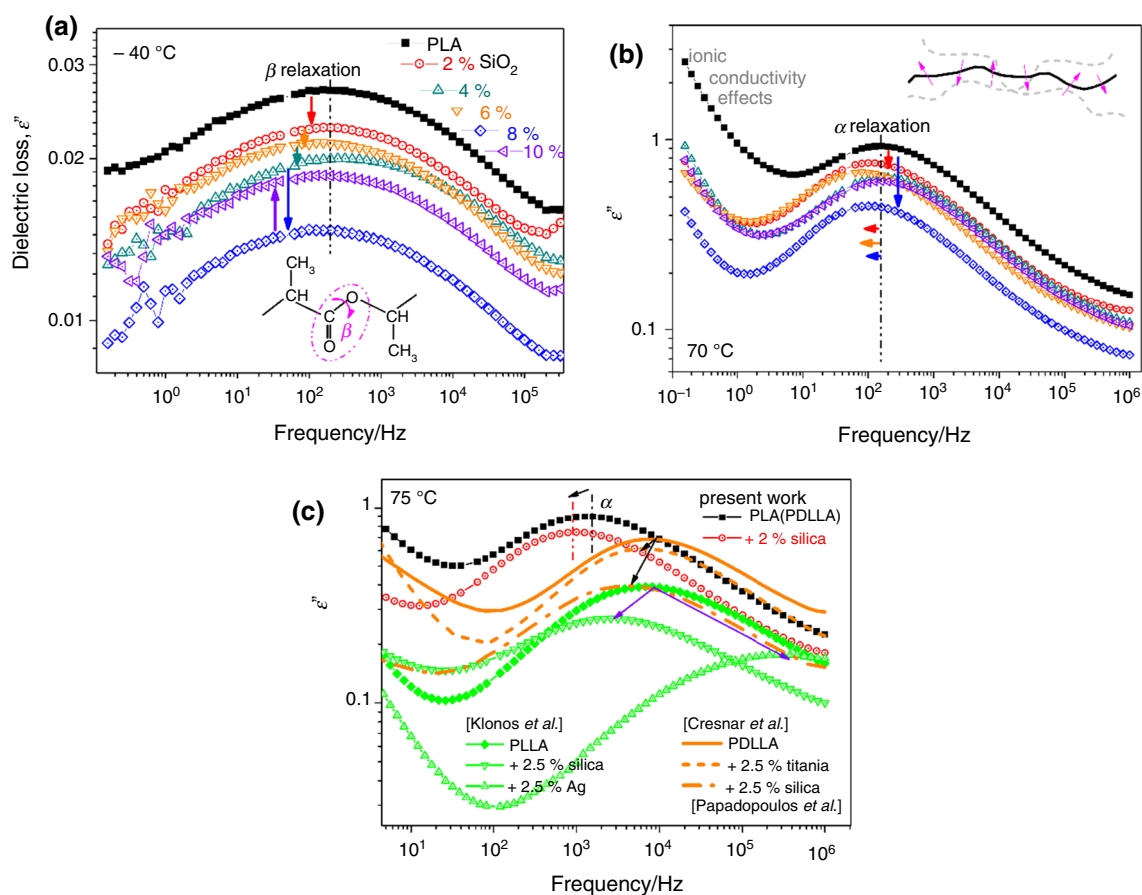
Fig. 11 Comparative BDS isothermal plots of the imaginary part of dielectric permittivity, ε'', against frequency, for all samples at the initially amorphous state at **a** $-40\,°C$ to focus on the local β relaxation and **b** $70\,°C$ focusing on the segmental/main α relaxation. **c** Shows the α relaxation at $75\,°C$ for neat PLA and PLA+2 wt% silica, more-over, compares the data by the present work with previous recordings on similar and different PLAs in bulk and in the form of nanocomposites filled with 2.5 mass% SiO_2 [25, 38], TiO_2 [33] and Ag [32, 38] nanoparticles

relaxation is followed as a relatively weak peak. β has been assigned [70, 71] to arise from dipole moments originating from the crankshaft motions of the carbonyl at the PLA backbone (inset scheme to Fig. 11a). At temperatures closely above T_g (rubbery state), the dielectric analogue of glass transition is recorded via a stronger $\varepsilon''(f)$ peak (Fig. 11b). This is the so-called α relaxation that originates from the segmental chains' motions, in particular, arising from the dipoles perpendicular to the chains (inset scheme to Fig. 11b). Up to about 85 °C in Figure S3, the magnitude of α decreases with temperature, as expected for amorphous polymers [43], whereas for further temperature increase, the relaxation exhibits a sharp strength suppression. This is due to the evolution of cold crystallization and occurs in all samples. In Fig. 11a, there are not recorded severe alternations in the f_{max} of β relaxation, with the case of PLA+4% silica showing slightly faster β (elevated f_{max}). Regarding α relaxation in Fig. 11b, the silica addition tends to decelerate the process, with the exception of PLA + 10% silica. These moderate effects on α are in general in agreement with the calorimetric findings for T_g.

In Fig. 11c, we compare some of the results for α of the present work with those on similar and quite different PLAs from previous studies [25, 32, 33, 38]. The intension is to show that independently from the type of PLA (l-/d-lactide ratio and molar mass) the weak or strong PLA/filler interfacial interactions result to decelerations of α, i.e., in the cases of metal oxide nanoparticles (SiO_2, TiO_2) which 'carry' many surface hydroxyls. On the other hand, in the case of absent direct interactions between the polymer and filler (e.g., Ag nanoparticles), accelerations can be recorded [32], for example, due to increase in the polymer free volume [24, 54].

Observing the raw data of Fig. 11a, b from another point of view (vertical arrows), it is interesting to note the almost systematic suppression of the relaxations' magnitude (area below the ε'' trace) in the PNCs. To further evaluate this, in terms of dielectric strength ($\Delta\varepsilon$), as well as the time scale, the BDS results were analyzed by 'critically' fitting to the experimental data [72] of a widely used model function to each process, namely the Havriliak–Negami (HN) [73] function (Eq. 4).

$$\varepsilon^*(f) = \varepsilon_\infty + \frac{\Delta\varepsilon}{\left(1 + \left(\frac{if}{f_0}\right)^{\alpha_{HN}}\right)^{\beta_{HN}}} \qquad (4)$$

In Eq. 4, f_0 is a characteristic frequency related to the frequency of maximum ε'', ε_∞ describes the value of ε' for $f \gg f_0$, while β_{HN} and α_{HN} are the shape parameters of relaxation for the symmetry and the width of relaxation times, respectively. An example of such fitting is demonstrated in a later figure.
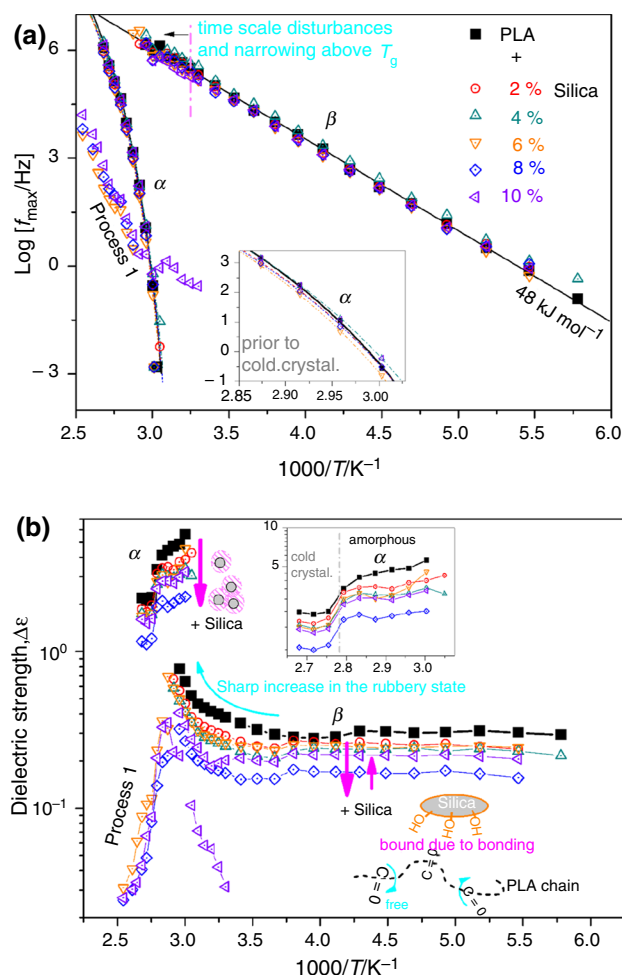
Fig. 12 **a** Arrhenius plots (dielectric relaxation map) and **b** dielectric strength, $\Delta\varepsilon$, for PLA and all nanocomposites in their initially amorphous state. The insets show more details of α relaxation. The added straight and curved lines in **a** are fittings of the Arrhenius and the VFTH equations, respectively

Combining the outcomes by the said fitting process, we constructed the overall dielectric relaxation map in Fig. 12, in terms of time scale (Arrhenius plots in Fig. 12a) and the reciprocal temperature dependence of $\Delta\varepsilon$ (Fig. 12b).

β relaxation shows a linear time scale in Fig. 12a which is the typical 'Arrhenius' behavior of local dynamics. The corresponding points could be fitted with the Arrhenius [43] Eq. 5,

$$f(T) = f_{0,Arrh} \cdot e^{-\frac{E_{act}}{kT}} \qquad (5)$$

by which the activation energy was estimated, $E_{act} \sim 48$ kJ mol^{-1} (0.5 eV).

According to the fitting results, at low temperatures β is symmetric and wide ($\alpha_{HN} \sim 0.2$ and $\beta_{HN} \sim 1$ in Eq. 4) and when temperature increases above T_g the same process becomes more narrow ($\alpha_{HN} \sim 0.3$–0.4, $\beta_{HN} \sim 1$), while its

$\Delta\varepsilon$ exhibits a strong increase (Fig. 12b). The results suggest decreased width of relaxation times, thus, increased homogeneity, and at the same time enhanced polarizability. Moreover, it is interesting that a local process senses the large scale structural change of the matrix, from glassy to rubbery. This is not trivial in the literature. However, we have recently discussed [24, 74] that similar situation between local and segmental mobility is recorded in PLA [24, 25] and other polyesters {polycaprolactones, poly(alkylene furanoate)s and poly(alkylene vanillate)s} [74, 75]. Therefore, we have proposed that the phenomenon is observed when the local relaxation arises from dipolar motions at the polymer backbone (ester groups, furan- or vanillic-rings). A final very interesting point on β is its almost systematic $\Delta\varepsilon$ suppression (Fig. 12b) with the addition of silica. Considering the molecular origins of β and the data by FTIR discussed in the previous (Fig. 2b), it is tempting to propose that this suppression is directly correlated to the interfacial PLA-silica interaction, which leads to a reduced fraction of free carbonyls and their corresponding dipoles.

α relaxation in the amorphous state is fitted better by an asymmetric HN term ($\alpha_{HN} \sim 0.6$ and $\beta_{HN} \sim 0.6$–0.7 in Eq. 4), while upon the involvement of cold crystallization, α weakens and changes to symmetric ($\beta_{HN} = 1$) and slightly wider ($\alpha_{HN} \sim 0.4$–0.5). These recordings are expected and come in accordance with previous studies [32, 45, 76, 77]. The time scale of α does not change significantly with composition, exhibiting only slight decelerations in almost all PNCs and a mild acceleration in PLA + 4% silica. The curved lines connecting the points of α in Fig. 12a are fittings of the Vogel–Fulcher–Tammann–Hesse (VFTH) model function [43] (Eq. 6), the characteristic behavior of cooperative dynamics.

$$f(T) = f_{0,\text{VFTH}} \cdot e^{-\frac{B}{T-T_0}} \tag{6}$$

In this equation, $f_{0,\text{VFTH}}$ is a frequency constant varying in the range 10^{12}–10^{14} Hz, T_0 is the so-called Vogel temperature and B is a material constant ($= D \cdot T_0$, where D is the so-called fragility strength parameter) [78]. After fitting Eq. 6 to the experimental data corresponding to the uncrystallized sample and fixing $f_{0,\text{VFTH}}$ to the phonon value 10^{13} Hz [41, 43, 61], we may obtain two values. First, the dielectric glass transition temperature, $T_{g,\text{diel}}$, as the extrapolated point of VFTH to the equivalent frequency of conventional calorimetry, i.e., $\sim 10^{-2.8}$ Hz (100 s) [43]. We may also estimate from the values for T_0 and D the fragility index of α relaxation, m_α, according to Eq. 7.

$$m_\alpha = 16 + 590/D \tag{7}$$

The results on $T_{g,\text{diel}}$ and m_α are shown as a function of silica loading in Fig. 13a. m_α equals 154 for neat PLA and drops in the PNCs almost systematically (145–147). This suggests reduced cooperativity of the bulk-like PLA in the PNCs, or else increase in the cooperativity length [43], most probably due to the additional constraints imposed by the presence of the fillers. The decrease in fragility in the amorphous state could be also one of the origins for the recorded thinner lamellae upon the crystals formation (XRD, Fig. 10a).

$T_{g,\text{diel}}$ does not significantly nor systematically vary between the different samples, as it scatters around 54 °C (neat PLA) by ± 1 K in Fig. 13a. We recall that the most systematic trend recorded in the calorimetric T_g, namely an increasing with silica by1–2 K, in addition to T_g being 3–4 K larger as compared to $T_{g,\text{diel}}$. The discrepancy between these different techniques suggests the decoupling between T_g and segmental dynamics. This has been found true also
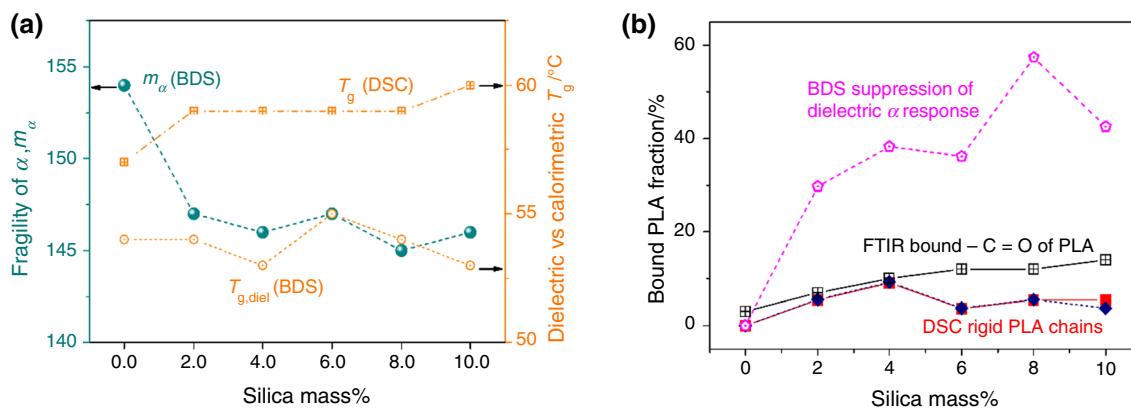
Fig. 13 a The NP loading dependence of (right axis) fragility index of α relaxation, m_α, being shown comparatively with (left-axis) the calorimetric and dielectric glass transition temperatures, T_g and $T_{g,\text{diel}}$, respectively. b The estimated bound PLA fraction based on the various techniques, BDS (at 70 °C), DSC and FTIR (details in the main text)

in previous works on various PNCs [33, 58, 79]. There has been proposed that the different T_gs are due to following quite different physical properties, large scale thermal-phase transition (DSC) against dipole moments relaxation (BDS) [58, 80]. This seems true in general in the cases of weak T_g changes related to more factors, such as the weak polymer chains flexibility, the low amounts of nanofillers and/or the low amounts of interfacial bound polymer [41, 62].

From the dielectric data on $\Delta\varepsilon$, in particular from the suppression of $\Delta\varepsilon$ of α relaxation (Fig. 12b), we performed an estimation of the 'dielectrically bound-rigid' amorphous polymer fraction (RAF_{BDS}), employing a 'two-phase' model as in DSC by an equivalent route (Eq. 8) [18, 32, 38].

$$RAF_{BDS}(\%) = \left(1 - MAF_{BDS}\right) \cdot 100 = \left(1 - \frac{\Delta\varepsilon_\alpha^{PNC}}{\Delta\varepsilon_\alpha^{MATRIX}}\right) \cdot 100$$

(8)

In Eq. 8, $\Delta\varepsilon_\alpha^{PNC}$ and $\Delta\varepsilon_\alpha^{MATRIX}$ are the dielectric strengths of α relaxation in the PNC and in neat PLA, respectively, at a temperature above T_g and below cold crystallization. This temperature was chosen here at 70 °C and, thus, the RAF_{BDS} values obviously correspond to amorphous samples. Please note that the employment of Eq. 8 implies the serious assumption that the polarizability of the mobile polymer chains [39, 80] is similar for the unfilled PLA and the PNCs. The data for RAF_{BDS} are shown in Fig. 13b comparatively with RAF by DSC and X_{FTIR} by FTIR. RAF_{BDS} shows an increasing trend with silica addition not being monotonic. The absolute values for RAF_{BDS} are significantly larger (30–57%) as compared to those for RAF by DSC (4–9%) and X_{FTIR} (3–14%), which could indicate the higher sensitivity of the dielectric technique.

Finally, we would like to report that due to the high resolving power of BDS in combination to the power of analysis [71, 72], an additional process could be resolved apart from β and α. This is the case of *process 1*, the existence of which is more clear even from some raw data, such as those of PLA + 10% silica (Fig. 14a). In the PNCs filled with 8 and 10% silica, *process 1* was necessary for the fitting of the overall frequency ε'' response. The process is exceptionally weak as compared to α (please see its low $\Delta\varepsilon$ in Fig. 12b) and could be unbiasly fitted ($\alpha_{HN} \sim 0.65$–0.7 and $\beta_{HN} = 1$, quite narrow HN) within only the said PNCs. The fitting was actually enabled by the simultaneously suppressed contributions of α and ionic conductivity contributions. The same process can be fitted also with the rest of the samples only via biased fitting. Therefore, it is not clear whether the process is related directly to the filler.

From the more solid results on *process 1*, we constructed the Arrhenius plots, being shown in Figs. 12a and 14b. Its time scale is almost linear and exhibits modes both slower and faster as compared to α relaxation. In
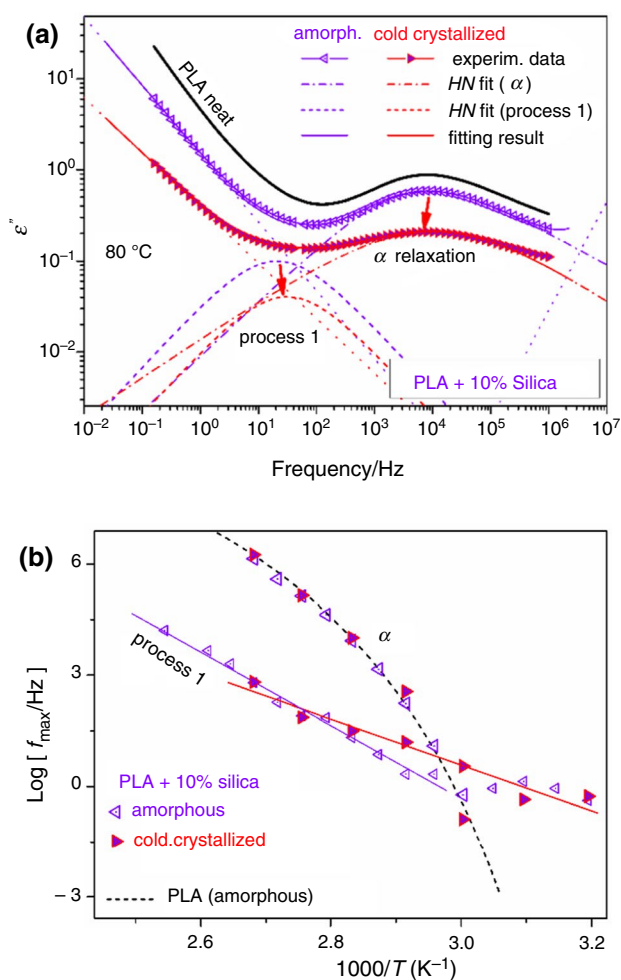
Fig. 14 The effects of crystallization on α relaxation and *process 1* as recorded **a** by the raw $\varepsilon''(f)$ spectra at 80 °C and the corresponding analysis as well as **b** in terms of the overall time scale—Arrhenius plots

PLA + 10% silica, the process was even more clear upon evolution of cold crystallization (Fig. 14a) and its $\Delta\varepsilon$ was suppressed similarly to that of α. The results suggest that *process 1* should possibly arise from the polymer rather the filler [47, 81], moreover, from the amorphous fraction of PLA. Similar dynamics and correlations of additional processes with α have been reported in PNCs of PLA and other polymer-based PNCs [24, 25, 35, 82, 83], in polymers in the form of thin films adsorbed at solid surfaces [84], in bulk polymers (e.g., atactic/syndiotactic polystyrene [85]) and, recently, in polystyrene single chain nanoparticles [86]. Among these works, three potential origins of *process 1* are involved, namely the dynamics of polymer chains spatially confined between nanoparticles [82], constrained dynamics in the adsorbed layer onto the solid surfaces [84] or dynamics of bulky chains of, however, special conformations (e.g., local fluctuations within

helical 'rods') [85]. Due to the limited data on this weak process here, we cannot securely conclude to its origins.

Interesting effects were recorded in this work; nevertheless, some questions regarding crystallinity, filler dispersion and molecular dynamics occurred. The employment of more advanced techniques on structure, for example, transmission electron microscopy, small angle X-ray scattering [87, 88] and fast scan chip calorimetry [17, 68, 87], could shed more light on the opened issues.

Conclusions

A series of new PLA-based PNCs filled with 2–10% fumed silica PNCs were prepared by solution casting and investigated. Interfacial interactions between the fillers and polymer were manifested, in particular, between the surface –OH and the PLA backbone –C=O. The degree of interaction was evaluated by three routes, namely directly via the disturbance of the carbonyl vibration in FTIR and indirectly via the formation of interfacial rigid amorphous chains by DSC and BDS. Additional indications were interestingly revealed by the suppression of local PLA dynamics, β relaxation that dielectrically screens the local crankshaft motion of the backbone carbonyl. The segmental mobility was found moderately decelerated in DSC (elevated T_g by 1–2 K) and mainly unaffected by BDS, with, however, the nanosilicas/PLA interactions were found responsible for imposing a decrease in the α process fragility. Coming to the effects of the nanofillers on PLA crystallization, which is developed only via cold crystallization for the said PLA (4% d-lactic, 75 kg mol^{-1} in molar mass), according to DSC, the fillers addition suppresses both the rate and the degree of crystallization. This suggests that the nanosilicas do not offer additional crystallization sites, which is not the common case in case of PLA-based PNCs. Interestingly, the results by PLM provide indications for an opposite behavior of the fillers, as more crystals seems to be developed in the PNCs. This initially contradictory behavior, was interpreted by a complex although realistic scenario. The latter involves the indirect filler effect (interactions) on slightly hindering molecular mobility, however, activating more of the PLA's endogenic nuclei. At the expenses of latter, the quality (density) of the crystals seems to be worse in the PNCs. As in previous works on PLA-based systems, this sustainable polymer seems to be a still promising and worth to study material, as it offers for variety of physical properties manipulation and, consequently, macroscopic performance (mechanical, small molecules permeation, heat transport, etc.).

Supplementary Information The online version contains supplementary material available at https://doi.org/10.1007/s10973-022-11716-7.

Declarations

References

1. Sperling LH. Introduction to physical polymer science. New Jersey: Wiley; 2005. https://doi.org/10.1002/0471757128.
2. Mark JE. Ceramic-reinforced polymers and polymer-modified ceramics. Polym Eng Sci. 1996;36:2905–20. https://doi.org/10.1002/pen.10692.
3. Bokobza L, Chauvin JP. Reinforcement of natural rubber: use of in situ generated silicas and nanofibres of sepiolite. Polymer. 2005;46:4144–51. https://doi.org/10.1016/j.polymer.2005.02.048.
4. Paul DR, Robeson LM. Polymer nanotechnology: nanocomposites. Polymer. 2008;49:3187–204. https://doi.org/10.1016/j.polymer.2008.04.017.
5. Jancar J, Douglas JF, Starr FW, Kumar SK, Cassagnau P, Lesser AJ, Sternstein SS, Buehler MJ. Current issues in research on structure–property relationships in polymer nanocomposites. Polymer. 2010;51:3321–43. https://doi.org/10.1016/j.polymer.2010.04.074.
6. Post W, Susa A, Blaauw R, Molenveld K, Knoop RJI. A review on the potential and limitations of recyclable thermosets for structural applications. Polym Rev. 2020;60:359–88. https://doi.org/10.1080/15583724.2019.1673406.
7. Casalini T, Rossi F, Castrovinci AL, Perale G. A perspective on polylactic acid-based polymers use for nanoparticles synthesis and applications. Front Bioeng Biotechnol. 2019;7:259. https://doi.org/10.3389/fbioe.2019.00259.
8. Ahmed J, Varshney SK. Polylactides-chemistry, properties and green packaging technology: a review. Int J Food Prop. 2011;14:37–58. https://doi.org/10.1080/10942910903125284.
9. Ngo TD, Kashani A, Imbalzano G, Nquyen KTQ, Hui D. Additive manufacturing (3D printing): a review of materials, methods, applications and challenges. Compos B Eng. 2018;143:172–96. https://doi.org/10.1016/j.compositesb.2018.02.012.
10. Matos BDM, Rocha V, da Silva EJ, Moro FH, Bottene AC, Ribeiro CA, Dias DDS, Antonio SG, do Amaral AC, Cruz SA, Barud HGDO, Barud HDS. Evaluation of commercially available polylactic acid (PLA) filaments for 3D printing applications. J Therm Anal Calorim. 2019;137:555–62. https://doi.org/10.1007/s10973-018-7967-3.
11. Garlotta D. A literature review of poly(lactic acid). J Polym Environ. 2001;9:63–84. https://doi.org/10.1023/A:1020200822435.
12. Saini P, Arora M, Kumar MNVR. Poly(lactic acid) blends in biomedical applications. Adv Drug Deliv Rev. 2016;107:47–59. https://doi.org/10.1016/j.addr.2016.06.014.

13. Saeidlou S, Huneault MA, Li H, Park CB. Poly(lactic acid) crystallization. Prog Polym Sci. 2012;37:1657–77. https://doi.org/10.1016/j.progpolymsci.2012.07.005.

14. Balla E, Daniilidis V, Karlioti G, Kalamas T, Stefanidou M, Bikiaris ND, Vlachopoulos A, Koumentakou I, Bikiaris DN. Poly(lactic acid) a versatile biobased polymer of next decades with multifunctional properties. From monomer synthesis, polymerization techniques and molecular weight increase to PLA applications. Polymers. 2021;13:1822. https://doi.org/10.3390/polym13111822.

15. Kontou E, Niaounakis M, Georgiopoulos P. Comparative study of PLA nanocomposites reinforced with clay and silica nanofillers and their mixtures. J Appl Polym Sci. 2011;122:1519–29. https://doi.org/10.1002/app.34234.

16. Androsch R, Naeem Iqbal HM, Schick C. Non-isothermal crystal nucleation of poly(l-lactic acid). Polymer. 2015;81:151–8. https://doi.org/10.1016/j.polymer.2015.11.006.

17. Toda A, Androsch R, Schick C. Insights into polymer crystallization and melting from fast chip calorimetry. Polymer. 2016;91:239–63. https://doi.org/10.1016/j.polymer.2016.03.038.

18. Terzopoulou Z, Klonos PA, Kyritsis A, Tziolas A, Avgeropoulos A, Papageorgiou GZ, Bikiaris DN. Interfacial interactions, crystallization and molecular mobility in nanocomposites of poly(lactic acid) filled with new hybrid inclusions based on graphene oxide and silica nanoparticles. Polymer. 2019;166:1–12. https://doi.org/10.1016/j.polymer.2019.01.041.

19. Raquez JM, Habibi Y, Murariu M, Dubois P. Polylactide (PLA)–based nanocomposites. Prog Polym Sci. 2013;38:1504–42. https://doi.org/10.1016/j.progpolymsci.2013.05.014.

20. Papageorgiou GZ, Terzopoulou Z, Bikiaris D, Triantafyllidis KS, Diamanti E, Gournis D, Klonos P, Giannoulidis E, Pissis P. Evaluation of the formed interface in biodegradable poly(l-lactic acid)/graphene oxide nanocomposites and the effect of nanofillers on mechanical and thermal properties. Thermochim Acta. 2014;597:48–57. https://doi.org/10.1016/j.tca.2014.10.007.

21. Tenn N, Follain N, Soulestin J, Crétois R, Bourbigot S, Marais S. Effect of nanoclay hydration on barrier properties of PLA/montmorillonite based nanocomposites. J Phys Chem C. 2013;117:12117–35. https://doi.org/10.1021/jp401546t.

22. Georgiopoulos P, Kontou E, Meristoudi A, Pispas S, Chatzinikolaidou M. The effect of silica nanoparticles on the thermomechanical properties and degradation behavior of polylactic acid. J Biomater Appl. 2014;29:662–74. https://doi.org/10.1177/0885328214545351.

23. Müeller AJ, Ávila M, Saenz G, Salazar J. Crystallization of PLA-based materials. In: Jiménez A, Peltzer M, Ruseckaite R, editors. Poly(lactic acid) and technology: processing, properties, additives and applications. Cambridge: RSC Publishing; 2015. https://doi.org/10.1039/9781782624806-00066.

24. Pušnik Črešnar K, Klonos PA, Zamboulis A, Terzopoulou Z, Xanthopoulou E, Papadopoulos L, Kyritsis A, Kuzmič K, Zemljič LF, Bikiaris DN. Structure–properties relationships in renewable composites based on polylactide filled with tannin and kraft lignin—crystallization and molecular mobility. Thermochim Acta. 2021;703: 178998. https://doi.org/10.1016/j.tca.2021.178998.

25. Papadopoulos L, Klonos PA, Tezopoulou Z, Psochia E, Sanusi OM, Aït Hocine N, Benelfellah A, Giliopoulos D, Triantafyllidis K, Kyritsis A, Bikiaris DN. Comparative study of crystallization, semicrystalline morphology, and molecular mobility in nanocomposites based on polylactide and various inclusions at low filler loadings. Polymer. 2021;217:123457. https://doi.org/10.1016/j.polymer.2021.123457.

26. Neratzaki M, Prokopiou L, Bikiaris DN, Patsiaoura D, Chrissafis K, Klonos P, Kyritsis A, Pissis P. In situ prepared poly(d,l-lactic acid)/silica nanocomposites: study of molecular composition, thermal stability, glass transition and molecular dynamics.

27. Thermochim Acta. 2018;669:16–29. https://doi.org/10.1016/j.tca.2018.08.025.

27. Androsch R, Zhuravlev E, Schick C. Solid-state reorganization, melting and melt-recrystallization of conformationally disordered crystals (α′-phase) of poly(l-lactic acid). Polymer. 2014;55:4932–41. https://doi.org/10.1016/j.polymer.2014.07.046.

28. Chen L, Dou Q. Influence of the combination of nucleating agent and plasticizer on the non-isothermal crystallization kinetics and activation energies of poly(lactic acid). J Therm Anal Calorim. 2020;139:1069–90. https://doi.org/10.1007/s10973-019-08507-y.

29. Righetti MC, Gazzano M, Di Lorenzo ML, Androsch R. Enthalpy of melting of α′- and α-crystals of poly(l-lactic acid). Eur Polym J. 2015;70:215–20. https://doi.org/10.1016/j.eurpolymj.2015.07.024.

30. Amini M, Ebadi-Dehaghani H. Non-isothermal crystallization and oxygen permeability of PP/PLA/EVOH ternary blends. J Therm Anal Calorim. 2018;132:1833–44. https://doi.org/10.1007/s10973-018-7084-3.

31. Klonos PA, Peoglos V, Bikiaris DN, Kyritsis A. Rigid amorphous fraction and thermal diffusivity in nanocomposites based on poly(l-lactic acid) filled with carbon nanotubes and graphene oxide. J Phys Chem C. 2020;123:5469–79. https://doi.org/10.1021/acs.jpcc.9b11843.

32. Klonos P, Terzopoulou Z, Koutsoumpis S, Zidropoulos S, Kripotou S, Papageorgiou GZ, Bikiaris D, Kyritsis A, Pissis P. Rigid amorphous fraction and segmental dynamics in nanocomposites based on poly(l-lactic acid) and nano-inclusions of 1–3D geometry studied by thermal and dielectric techniques. Eur Polym J. 2016;82:16–34. https://doi.org/10.1016/j.eurpolymj.2016.07.002.

33. Pušnik Črešnar K, Zemljič LF, Papadopoulos L, Terzopoulou Z, Zamboulis A, Klonos PA, Bikiaris DN, Kyritsis A, Pissis P. Effects of Ag, ZnO and TiO₂ nanoparticles at low contents on the crystallization, semicrystalline morphology, interfacial phenomena and segmental dynamics of PLA. Mater Today Commun. 2021;27: 102192. https://doi.org/10.1016/j.mtcomm.2021.102192.

34. Klonos PA, Papadopoulos L, Papageorgiou GZ, Kyritsis A, Pissis P, Bikiaris DN. Interfacial interactions, crystallization, and molecular dynamics of renewable poly(propylene furanoate) in situ filled with initial and surface modified carbon nanotubes and graphene oxide. J Phys Chem C. 2020;124:10220–34. https://doi.org/10.1021/acs.jpcc.0c01313.

35. Klonos PA, Papadopoulos L, Terzopoulou Z, Papageorgiou GZ, Kyritsis A, Bikiaris DN. Molecular dynamics in nanocomposites based on renewable poly(butylene 2,5-furan-dicarboxylate) in situ reinforced by montmorillonite nanoclays: effects of clay modification, crystallization, and hydration. J Phys Chem B. 2020;124:7306–17. https://doi.org/10.1021/acs.jpcb.0c04306.

36. Klonos P, Sulym IY, Sternik D, Konstantinou P, Goncharuk OV, Deryło-Marczewska A, Gun'ko VM, Kyritsis A, Morphology PP. crystallization and rigid amorphous fraction in PDMS adsorbed onto carbon nanotubes and graphite. Polymer. 2018;139:130–44. https://doi.org/10.1016/j.polymer.2018.02.020.

37. Ming Y, Zhou Z, Hao T, Nie Y. Polymer nanocomposites: role of filler content and interfacial interaction on crystallization. Eur Polym J. 2022;162:110894. https://doi.org/10.1016/j.eurpolymj.2021.110894.

38. Klonos P, Pissis P. Effects of interfacial interactions and of crystallization on rigid amorphous fraction and molecular dynamics in polylactide/silica nanocomposites: a methodological approach. Polymer. 2017;112:228–43. https://doi.org/10.1016/j.polymer.2017.02.003.

39. Füllbrandt M, Purohit PJ, Schönhals A. Combined FTIR and dielectric investigation of poly(vinyl acetate) adsorbed on silica particles. Macromolecules. 2013;46:4626–32. https://doi.org/10.1021/ma400461p.

40. Wurm A, Ismail M, Kretzschmar B, Pospiech D, Schick C. Retarded crystallization in polyamide/layered silicates nanocomposites caused by an immobilized interphase. Macromolecules. 2010;43:1480–7. https://doi.org/10.1021/ma902175r.

41. Klonos, P.; Kulyk, K.; Borysenko, M. V.; Gun'ko, V. M.; Kyritsis, A.; Pissis, P. Effects of molecular weight below the entanglement threshold on interfacial nanoparticles/polymer dynamics. *Macromolecules* **2016**, *49*, 9457–9473. https://doi.org/10.1021/acs.macromol.6b01931

42. Dobbertin J, Hannemann J, Schick C, Pötter M, Dehne H. Molecular dynamics of α-relaxation during crystallization of a low-molecular-weight compound: a real-time dielectric spectroscopy study. J Chem Phys. 1998;108:9062. https://doi.org/10.1063/1.476352.

43. Kremer F, Schönhals A, editors. Broadband dielectric spectroscopy. New York: Springer; 2003. https://doi.org/10.1007/978-3-642-56120-7.

44. Hendricks J, Louhichi A, Metri V, Fournier R, Reddy N, Bouteiller L, Cloitre M, Clasen C, Vlassopoulos D, Briels WJ. Nonmonotonic stress relaxation after cessation of steady shear flow in supramolecular assemblies. Phys Rev Lett. 2019;123: 218003. https://doi.org/10.1103/PhysRevLett.123.218003.

45. Brás AR, Dionisio M, Mano JF. Influence of crystallinity in molecular motions of poly(L-lactic acid) investigated by dielectric relaxation spectroscopy. Macromolecules. 2008;41:6419–30. https://doi.org/10.1021/ma800842a.

46. Guo T, Zhou S, Zheng X, Jiang J. Modeling and investigation of interfacial interaction between PLA and one type of deficient hydroxyapatite. J Phys Chem A. 2009;113:7112–23. https://doi.org/10.1021/jp9017234.

47. Klonos PA. Dynamics of molecules physically adsorbed onto metal oxide nanoparticles: similarities between water and a flexible polymer. J Phys Chem C. 2018;122:28825–9929. https://doi.org/10.1021/acs.jpcc.8b10043.

48. Zhou S, et al. Hydrogen Bonding Interaction of poly(d,l-lactide)/hydroxyapatite nanocomposites. Chem Mater. 2007;19:247–53. https://doi.org/10.1021/cm0619398.

49. Dollase T, Spiess HW, Gottlieb M, Yerushalmi-Rosen R. Crystallization of PDMS: the effect of physical and chemical crosslinks. Europhys Lett. 2002;60:390–6. https://doi.org/10.1209/epl/i2002-00276-4.

50. Carrillo JMY, Cheng S, Kumar R, Goswami R, Sokolov AP, Sumpter BG. Untangling the effects of chain rigidity on the structure and dynamics of strongly adsorbed polymer melts. Macromolecules. 2015;48:4207–19. https://doi.org/10.1021/acs.macromol.5b00624.

51. Hodge IM. Effects of annealing and prior history on enthalpy relaxation in glassy polymers 6 Adam–Gibbs formulation of nonlinearity. Macromolecules. 1987;20:2897–908. https://doi.org/10.1021/ma00177a044.

52. Cowie JMG, Harris S, Gómez Ribelles JL, Meseguer JM, Romero F, Torregrosa C. Glass transition and structural relaxation in polystyrene/poly(2,6-dimethyl-1,4-phenylene oxide) miscible blends. Macromolecules. 1999;32:4430–8. https://doi.org/10.1021/ma971531j.

53. Alves NM, Mano JF, Balaquer E, Meseguer Dueñas JM, Gómez Ribelles JL. Glass transition and structural relaxation in semicrystalline poly(ethylene terephthalate): a DSC study. Polymer. 2002;43:4111–22. https://doi.org/10.1016/S0032-3861(02)00236-7.

54. Boucher VM, Cangialosi D, Alegrìa A, Colmenero J, González-Irun J, Liz-Marzan LM. Physical aging in PMMA/silica nanocomposites: enthalpy and dielectric relaxation. J Non-Cryst Solids. 2011;357:605–9. https://doi.org/10.1016/j.jnoncrysol.2010.05.091.

55. Fischer EW, Sterzel HJ, Wegner G. Investigation of the structure of solution grown crystals of lactide copolymers by means of chemical reactions. Kolloid-Zeitschrift und Zeitschrift für Polymere. 1973;251:980–90. https://doi.org/10.1007/BF01498927.

56. Sargsyan A, Tonoyan A, Davtyan S, Schick C. The amount of immobilized polymer in PMMA SiO2 nanocomposites determined from calorimetric data. Eur Polym J. 2007;43:3113–27. https://doi.org/10.1016/j.eurpolymj.2007.05.011.

57. Szymoniak P, Li Z, Wang DY, Schönhals A. Dielectric and flash DSC investigations on an epoxy based nanocomposite system of MgAl layered double hydroxide as nanofiller. Thermochim Acta. 2019;677:151–61. https://doi.org/10.1016/j.tca.2019.01.010.

58. Koutsoumpis S, Raftopoulos KN, Oguz O, Papadakis CM, Menceloglu YZ, Pissis P. Dynamic glass transition of the rigid amorphous fraction in polyurethane-urea/SiO2 nanocomposites. Soft Matter. 2017;13:4580–90. https://doi.org/10.1039/C7SM00397H.

59. Leng J, Szymoniak P, Kang NJ, Wang DY, Wurm A, Schick C, Schönhals A. Influence of interfaces on the crystallization behavior and the rigid amorphous phase of poly(L-lactide)-based nanocomposites with different layered double hydroxides as nanofiller. Polymer. 2019;184: 121929. https://doi.org/10.1016/j.polymer.2019.121929.

60. Mizumo M, Nakamura K, Konishi T, Fukao K. Glass transition and thermal expansivity in silica-polystyrene nanocomposites. J Non-Cryst Solids. 2011;357:594–7. https://doi.org/10.1016/j.jnoncrysol.2010.06.061.

61. Fragiadakis D, Pissis P. Glass transition and segmental dynamics in poly(dimethyl siloxane)silica nanocomposites atudied by various techniques. J Non-Cryst Solids. 2007;353:4344–52. https://doi.org/10.1016/j.jnoncrysol.2007.05.183.

62. Klonos PA, Nosach LV, Voronin EF, Pakhlov EM, Kyritsis A, Pissis P. Glass transition and molecular dynamics in core–shell-type nanocomposites based on fumed silica and polysiloxanes: comparison between poly(dimethylsiloxane) and poly(ethylhydrosiloxane). J Phys Chem C. 2019;123:28427–36. https://doi.org/10.1021/acs.jpcc.9b07247.

63. Leng J, Purohit PJ, Kang N, Wang DY, Falkenhagen J, Emmerling F, Thünemann AF, Schönhals A. Structure-property relationships of nanocomposites based on polylactide and MgAl layered double hydroxides. Eur Polym J. 2015;68:338–54. https://doi.org/10.1016/j.eurpolymj.2015.05.008.

64. Androsch R, Zhang R, Schick C. Melt-recrystallization of poly(L-lactic acid) initially containing α′-crystals. Polymer. 2019;176:227–35. https://doi.org/10.1016/j.polymer.2019.05.052.

65. Delpouve N, Saiter A, Dargent E. Cooperativity length evolution during crystallization of poly(lactic acid). Eur Polym J. 2011;47:2414–23. https://doi.org/10.1016/j.eurpolymj.2011.09.027.

66. Zhuravlev E, Wurm A, Pötschke P, Androsch R, Schmelzer JWP, Schick C. Kinetics of nucleation and crystallization of poly(ε-caprolactone)—smultiwalled carbon nanotube composites. Eur Polym J. 2014;52:1–11. https://doi.org/10.1016/j.eurpolymj.2013.12.015.

67. Xu H, Cebe P. Heat capacity study of isotactic polystyrene: dual reversible crystal melting and relaxation of rigid amorphous fraction. Macromolecules. 2004;37:2797–806. https://doi.org/10.1021/ma035961n.

68. Monnier X, Cavallo D, Righetti MC, Di Lorenzo ML, Marina S, Martin J, Cangialosi D. Physical aging and glass transition of the rigid amorphous fraction in poly(l-lactic acid). Macromolecules. 2020;53:8741–50. https://doi.org/10.1021/acs.macromol.0c01182.

69. Papadopoulos L, Klonos PA, Tzetzis D, Papageorgiou GZ, Kyritsis A, Bikiaris DN. Effects of graphene nanoplatelets on crystallization, mechanical performance and molecular dynamics of the

renewable poly(propylene furanoate). Polymer. 2020;189: 122172. https://doi.org/10.1016/j.polymer.2020.122172.

70. Ren J, Urakawa O, Adachi K. Dielectric study on dynamics and conformations of poly(d,l-lactic acid) in dilute and semi-dilute solutions. Polymer. 2003;44:847–55. https://doi.org/10.1016/S0032-3861(02)00817-0.

71. Mierzwa M, Floudas G, Dorgan J, Knauss D, Wegner J. Local and global dynamics of polylactides. A dielectric spectroscopy study. J Non-Cryst Solids. 2002;307–310:296–303. https://doi.org/10.1016/S0022-3093(02)01480-1.

72. Jeszka JK, Pietrzak L, Pluta M, Boiteux G. Dielectric properties of polylactides and their nanocomposites with montmorillonite. J Non-Cryst Solids. 2010;356:818–21. https://doi.org/10.1016/j.jnoncrysol.2009.06.057.

73. Havriliak S, Negami S. A complex plane representation of dielectric and mechanical relaxation processes in some polymers. Polymer. 1967;8:161–210. https://doi.org/10.1016/0032-3861(67)90021-3.

74. Kourtidou D, Klonos PA, Papadopoulos L, Kyritsis A, Bikiaris DN, Chrissafis K. Molecular mobility and crystallization of renewable poly(ethylene furanoate) in situ filled with carbon nanotubes and graphene nanoparticles. Soft Matter. 2021;17:5815–28. https://doi.org/10.1039/D1SM00592H.

75. Xantopoulou E, Klonos PA, Zamboulis A, Terzopoulou Z, Kyritsis A, Pissis P, Bikiaris BN, Papageorgiou GZ. Molecular mobility investigation of the biobased poly(ethylene vanillate) and poly(propylene vanillate). Polymer. 2021;233: 124197. https://doi.org/10.1016/j.polymer.2021.124197.

76. Brás AR, Viciosa MT, Wang Y, Dionisio M, Mano JF. Crystallization of poly(l-lactic acid) probed with dielectric relaxation spectroscopy. Macromolecules. 2006;39:6513–20. https://doi.org/10.1021/ma061148r.

77. Wang Y, Funari SS, Mano JF. Influence of semicrystalline morphology on the glass transition of poly(l-lactic acid). Macrom Chem Phys. 2006;207:1262–71. https://doi.org/10.1002/macp.200600114.

78. Böhmer R, Ngai K, Angell CA, Plazek DJ. Nonexponential relaxations in strong and fragile glass formers. J Chem Phys. 1993;99:4201–9. https://doi.org/10.1063/1.466117.

79. Cangialosi D, Boucher VM, Alegría A, Colmenero J. Enhanced physical ageing of polymer nanocomposites: the key role of the area to volume ratio. Polymer. 2012;53:1362–72. https://doi.org/10.1016/j.polymer.2012.01.033.

80. Purohit PJ, Wang D, Wurm A, Schick C, Schönhals A. Comparison of thermal and dielectric spectroscopy for nanocomposites based on polypropylene and layered double hydroxide—proof of interfaces. Eur Polym J. 2014;55:48–56. https://doi.org/10.1016/j.eurpolymj.2014.03.005.

81. Cerveny S, Schwartz GA, Otegui J, Colmenero J, Loichen J, Westermann S. Dielectric study of hydration water in silica nanoparticles. J Phys Chem C. 2012;116:24340–9. https://doi.org/10.1021/jp307826s.

82. Elmahdy MM, Chrissopoulou K, Afratis A, Floudas G, Anastasiadis SH. Effect of confinement on polymer segmental motion and ion mobility in PEO/layered silicate nanocomposites. Macromolecules. 2006;39:5170–3. https://doi.org/10.1021/ma0608368.

83. Koutsoumpis S, Klonos P, Raftopoulos KN, Papadakis CM, Bikiaris D, Pissis P. Morphology, thermal properties and molecular dynamics of syndiotactic polystyrene (s-PS) nanocomposites with aligned graphene oxide and graphene nanosheets. Polymer. 2018;153:548–57. https://doi.org/10.1016/j.polymer.2018.08.052.

84. Madkour S, Szymoniak P, Heidari M, Klitzing V, R,.; Schönhals, A,. Unveiling the dynamics of self-assembled layers of thin films of poly(vinyl methyl ether) (PVME) by nanosized relaxation spectroscopy. ACS Appl Mater Interfaces. 2017;9:7535–46. https://doi.org/10.1021/acsami.6b14404.

85. Lupaşcu V, Picken SJ, Wübbenhorst M. Dynamics of T_2G_2 helices in atactic and syndiotactic polystyrene: new evidence from dielectric spectroscopy and FTIR. Macromolecules. 2006;39:5152–8. https://doi.org/10.1021/ma0606758.

86. Klonos PA, Patelis N, Glynos E, Sakellariou G, Kyritsis A. Molecular dynamics in polystyrene single-chain nanoparticles. Macromolecules. 2019;52:9334–40. https://doi.org/10.1021/acs.macromol.9b02070.

87. Szymoniak P, Qu X, Abbasi M, Pauw BR, Henning S, Li Z, Wang DY, Schick C, Saalwächter K, Schönhals A. Spatial inhomogeneity, interfaces and complex vitrification kinetics in a network forming nanocomposite. Soft Matter. 2021;17:2775–90. https://doi.org/10.1039/D0SM01992E.

88. Szymoniak P, Pauw BR, Qu X, Abbasi M, Schönhals A. Competition of nanoparticle-induced mobilization and immobilization effects on segmental dynamics of an epoxy-based nanocomposite. Soft Matter. 2020;16:5406–21. https://doi.org/10.1039/D0SM00744G.